Technical Report

Discovering small-molecule senolytics with deep neural networks

Felix Wong[1,2,3,7]**, Satotaka Omori**[2,3,4,7]**, Nina M. Donghia**[1,5]**, Erica J. Zheng**[2,6] **& James J. Collins** [1,2,5] ✉

The accumulation of senescent cells is associated with aging, inflammation and cellular dysfunction. Senolytic drugs can alleviate age-related comorbidities by selectively killing senescent cells. Here we screened 2,352 compounds for senolytic activity in a model of etoposide-induced senescence and trained graph neural networks to predict the senolytic activities of >800,000 molecules. Our approach enriched for structurally diverse compounds with senolytic activity; of these, three drug-like compounds selectively target senescent cells across different senescence models, with more favorable medicinal chemistry properties than, and selectivity comparable to, those of a known senolytic, ABT-737. Molecular docking simulations of compound binding to several senolytic protein targets, combined with time-resolved fluorescence energy transfer experiments, indicate that these compounds act in part by inhibiting Bcl-2, a regulator of cellular apoptosis. We tested one compound, BRD-K56819078, in aged mice and found that it significantly decreased senescent cell burden and mRNA expression of senescence-associated genes in the kidneys. Our findings underscore the promise of leveraging deep learning to discover senotherapeutics.

Cellular senescence is a permanent state of cell cycle arrest that is associated with cellular stress and aging. Although senescence primarily protects against cancer, senescent cells (Sncs) exhibit altered phenotypes and secrete senescence-associated secretory phenotype factors, which include cytokines, chemokines, growth factors and proteases that cause inflammation and tumorigenesis[1,2]. These factors, in turn, contribute to aging and the deleterious consequences of late-life diseases, including cancer, atherosclerosis and osteoarthritis. Recent studies have shown that the selective clearance of Sncs can ameliorate pathophysiological consequences associated with senescence[3–5]. In particular, senolytics, an emerging class of drugs that selectively kill Sncs, have been shown to extend healthspan and enhance the efficacy of chemotherapy in mice[5–10]. Yet, the removal of Sncs in mice has also

been shown to slow wound healing[11] and induce liver and perivascular tissue fibrosis[12], highlighting the need to discover senolytic therapies that do not induce severe side effects.

Given the potential of senolytics with few side effects to mediate healthy aging, there has been considerable interest in discovering novel senolytics. The first senolytics—dasatinib, quercetin, fisetin and ABT-263—emerged in the mid-2010s from targeted bioinformatics approaches that focused on pathways protecting Sncs from apoptosis[13–16]. Subsequently, senolytics including heat shock protein (HSP)-90 inhibitors[6], cardiac glycosides[7,17] and bromodomain and extra-terminal domain (BET) family protein inhibitors[8] have been discovered through high-throughput screens and detailed mechanistic studies. Many of these known senolytics have side effects or

[1]Institute for Medical Engineering & Science and Department of Biological Engineering, Massachusetts Institute of Technology, Cambridge, MA, USA. [2]Infectious Disease and Microbiome Program, Broad Institute of MIT and Harvard, Cambridge, MA, USA. [3]Integrated Biosciences, Inc, San Carlos, CA, USA. [4]Division of Cancer Cell Biology, Institute of Medical Science, The University of Tokyo, Minato-Ku, Tokyo, Japan. [5]Wyss Institute for Biologically Inspired Engineering, Harvard University, Boston, MA, USA. [6]Program in Chemical Biology, Harvard University, Cambridge, MA, USA. [7]These authors contributed equally: Felix Wong, Satotaka Omori. ✉e-mail: jimjc@mit.edu

limitations to clinical application. For instance, senolytics including fisetin and ABT-737 have limited bioavailability, and the evaluation of ABT-263 in phase II studies for the treatment of lung carcinoma revealed that thrombocytopenia and neutropenia were common side effects in patients[18]. Thus, the identification of novel senolytic compounds is needed to advance the development of senolytics as a class of therapeutics.

Parallel to the discovery and development of senolytics, machine learning has proven versatile for facilitating drug discovery efforts[19–22]. Various machine learning models have combined training data generated from biological screens or available from public databases with architectures including neural networks to predict the activities and pharmacological properties of chemical compounds[23–25], discover molecular binding targets and aging biomarkers[26–30], and design molecules that satisfy predetermined criteria for biological activity and physicochemical properties[31–33]. While machine learning approaches have successfully enabled the discovery of chemical compounds targeting diverse indications, including bacterial infection[23,24] and fibrosis[31], they remain to be developed, tested and applied in different therapeutic areas, including senolytics. In such applications, the design of appropriate conceptual frameworks, the generation of well-controlled training data, the choice of suitable model architectures, and the experimental validation of model predictions are important for determining a model's predictive accuracy and demonstrating the utility of machine learning for chemical compound discovery.

In this Technical Report, we reasoned that senolytic activity could be predicted in silico by machine learning models on the basis of chemical structure alone (Fig. 1a). We hypothesized that deep learning models could augment high-throughput screening efforts and identify senolytic compounds from vast chemical spaces, as we have previously demonstrated for antibiotics[23]. To this end, we trained a graph neural network platform with the results of a screen for senolytic activity of 2,352 compounds and applied it to predict senolytic activity in a chemical space of 804,959 compounds. In contrast to other architectures, graph neural networks enable molecular structures to be directly processed for training and prediction, and this architecture has previously been shown to improve predictive power[23,34]. After curating and testing an additional 266 compounds, our approach produced a working hit rate (positive predictive value) of 11.6%, enriching for structurally diverse senolytic compounds with favorable medicinal chemistry properties. Detailed studies of three selective compounds demonstrated that these compounds are effective senolytics (half-maximal inhibitory concentration, IC_{50} <20 μM) and exhibit selectivity comparable to that of ABT-737 in different senescence models. In order to identify potential mechanisms of action of the identified compounds, we combined molecular docking simulations involving well-studied senolytic protein targets with time-resolved fluorescence energy transfer (TR-FRET) experiments, which together suggest that the compounds act in part by binding Bcl-2. Furthermore, we found that the identified compounds have encouraging safety profiles in initial toxicity tests and tested one compound, BRD-K56819078, in aged mice, finding that it reduces senescent cell burden and senescence-associated messenger RNA (mRNA) expression in the kidneys. These results demonstrate the utility of graph neural networks for facilitating the identification of promising senolytic compounds, paving the way for effective senotherapeutics to be discovered using deep learning.

Results

Chemical screens of 2,352 compounds identify senolytics

To identify compounds with senolytic activity used to train our model, we first screened 2,352 compounds, largely from a library of US Food and Drug Administration-approved drugs and drugs undergoing clinical trials, for senolytic activity in a model of therapy-induced senescence (Methods). As a well-studied model system, human lung (IMR-90) fibroblasts were treated with etoposide to induce senescence via the
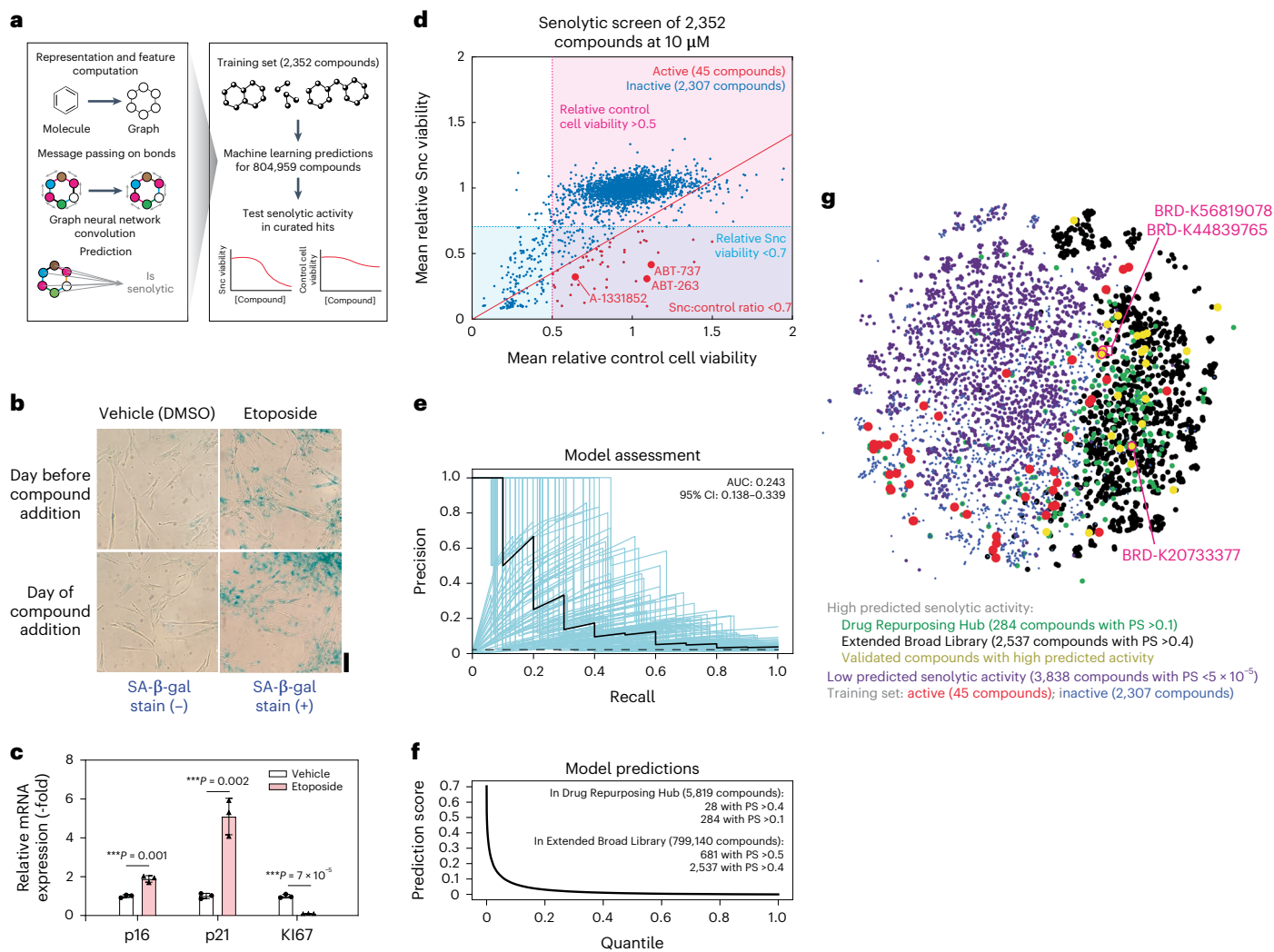
formation of double-stranded DNA breaks, and cells were allowed to recover in etoposide-free medium. We confirmed senescence by staining for senescence-associated β-galactosidase (SA-β-gal) at timepoints corresponding to 1 day before compound treatment and the day of compound treatment, which indicated substantively increased straining in etoposide-treated Sncs relative to vehicle (0.5% dimethyl sulfoxide (DMSO))-treated controls (Fig. 1b). Complementing these observations of SA-β-gal staining, we quantified p16, p21 and KI67 mRNA levels using quantitative PCR (Fig. 1c). Increased p16 and p21 mRNA levels are associated with senescence[35–38], and decreased mRNA levels of KI67, a proliferation marker, are associated with growth arrest[39,40]. Our measurements indicated at least onefold increases (p16 and p21) and decreases (KI67) in mRNA levels in Sncs relative to vehicle-treated controls (Fig. 1c). Sncs were then treated with 10 μM of each compound, and relative viability was measured by reduction of resazurin, a metabolic indicator, after a 3-day course of treatment (Extended Data Fig. 1 and Supplementary Data 1). As controls, vehicle-treated cells were counter-screened in the same way.

As a starting point for senolytic activity, we defined active compounds as those for which relative Snc viability was <0.5, relative viability of control cells was >0.5 and the ratio of relative Snc/control viability was <0.7 (Fig. 1d). Requiring the relative viability of control cells to be >0.5 ensured that active compounds are not strongly cytotoxic, while requiring the ratio of relative Snc/control viability to be <0.7 ensured that active compounds have at least moderate selectivity against Sncs. With these criteria, 45 compounds emerged as active from our initial screens (Fig. 1d). These compounds included known senolytics such as ABT-737, ABT-263, A-1331852, A-1155463 and ouabain. We further validated a subset of the active compounds by performing detailed dose–response measurements, which demonstrated that these compounds exhibit therapeutic indices against Sncs—that is, the ratio of Snc to control cell IC_{50} values—ranging from 1.5 (weakly selective) to 24.5 (selective) and IC_{50} values against Sncs ranging from 0.32 to 25.1 μM (Extended Data Fig. 2). To explore the effects of different screening concentrations on the identification of active compounds, we repeated the screen with treatment at 1 μM and found substantially fewer—only six—active compounds, which did not include known senolytics (Extended Data Fig. 2 and Supplementary Data 1). While these findings highlight the importance of screening at appropriate compound concentrations, we also note that our screening criteria provide only a starting point for defining senolytic activity: it is likely that not all active compounds identified here are true senolytics. Conversely, not all known senolytics emerge as active compounds in our screen, which may be due in part to the fact that several known senolytics are not selective at our screening concentrations of 1 and 10 μM (Supplementary Data 1).

On the basis of the foregoing criteria for active compounds, our screen at 10 μM revealed more active compounds, including known senolytics, than our screen at 1 μM. We therefore focused on using our screening results at 10 μM to train subsequent models. Due to the relatively small number of active compounds identified in our 10 μM screen, we reasoned that these data may be insufficient to accurately train detailed regression models; we therefore focused on developing binary classifier models, as we have previously done[23]. Nevertheless, as detailed further in Supplementary Note 1 and Supplementary Tables 1–11, additional analyses suggest that our model's predictive performance is robust to variation in the criteria used to define active compounds and the type of classifier used.

Design and validation of graph neural network models

We next used our screening data to train deep learning models that predict senolytic activity on the basis of chemical structure. Building on our work in antibiotic discovery[23], we employed message-passing graph neural network models[34]. Message-passing graph neural networks are a type of supervised model that takes as input a chemical structure of a molecule, integrates local information contained at each atom and

a

b

c

d

e

f

g

High predicted senolytic activity:
Drug Repurposing Hub (284 compounds with PS >0.1)
Extended Broad Library (2,537 compounds with PS >0.4)
Validated compounds with high predicted activity
Low predicted senolytic activity (3,838 compounds with PS <5 × 10⁻⁵)
Training set: active (45 compounds); inactive (2,307 compounds)

Fig. 1 | Graph neural networks predict senolytic activity. a, Schematic of the approach. A total of 2,352 compounds, including known senolytics, are screened for senolytic activity, and the data are used to train graph neural networks. Trained models are applied to predict the senolytic activities of 804,959 compounds. Compounds predicted to be active are tested for senolytic activity. **b,** SA-β-gal staining of vehicle- (0.5% DMSO) and etoposide-treated IMR-90 cells plated on the day before and day of compound addition. Each image represents two biological replicates. Scale bar, 100 μm. **c,** Relative mRNA expression of p16, p21 and KI67 in vehicle- (0.5% DMSO) and etoposide-treated IMR-90 cells on the day of compound addition. Data from three biological replicates are shown (black points), and bars represent average values. Error bars indicate one standard deviation. Two-sided two-sample *t*-test for differences in mean value: ***P < 0.005. **d,** Senolytic screening results for 2,352 compounds at a final concentration of 10 μM. Values show the mean of two biological replicates, and viability measurements are normalized by the interquartile mean of each

plate. Active compounds (red points) are those for which relative control cell viability is >0.5, relative Snc viability is <0.7, and the ratio of Snc to control cell viability is <0.7. All other compounds are inactive (blue points). Three known senolytics, ABT-737, ABT-263 and A-1331852, are highlighted (large red points). Sncs were induced with etoposide, and control cells were treated with vehicle (0.5% DMSO). **e,** Precision–recall curves for ten Chemprop models trained and tested on the data in **d**. The black dashed curve represents the baseline fraction of active compounds in the training set (1.9%). Blue curves and the 95% confidence interval (CI) indicate the variation generated by bootstrapping. AUC, area under the curve. **f,** Rank-ordered prediction scores (PS) of 804,959 compounds, for 20 Chemprop models trained on all the data in **d**. **g,** t-SNE plot of compounds with high and low predicted senolytic activity and the training set shown in **d**. Validated compounds refer to Fig. 2. Three validated compounds with high predicted activity, which we focus on in this study, and their corresponding identifiers are highlighted in magenta.

bond, and produces as output a prediction score representing the probability that the molecule possesses a property of interest. This model architecture has been shown to accurately predict properties, including antibiotic activity[23], toxicity[34] and side effects of drugs[34]. We assessed the ability of these models to predict senolytic activity by training and testing on 80–20 splits of our screening data. We then generated precision–recall curves, which plot the true positive rate against the positive predictive value (Fig. 1e). We found that the area under the precision–recall curve (auPRC), which measures the ability of the model to correctly identify a senolytic compound, was favorable, with a value of 0.24 (95% confidence internal 0.14–0.34). This indicates

that the model can more accurately identify senolytic compounds in our training set as compared to random (auPRC of 0.019). In contrast, alternative models based on random forests resulted in reduced performance, with at most an auPRC of 0.15 (Extended Data Fig. 3). Additional benchmarks of model performance using different metrics, including the positive predictive value at different prediction score thresholds, similarly indicated better performance in the graph neural network model (Supplementary Note 1).

Satisfied with the performance of our model, we retrained it using our entire screening dataset, and applied it to predict the senolytic activities of 804,959 compounds comprising the Broad Institute's
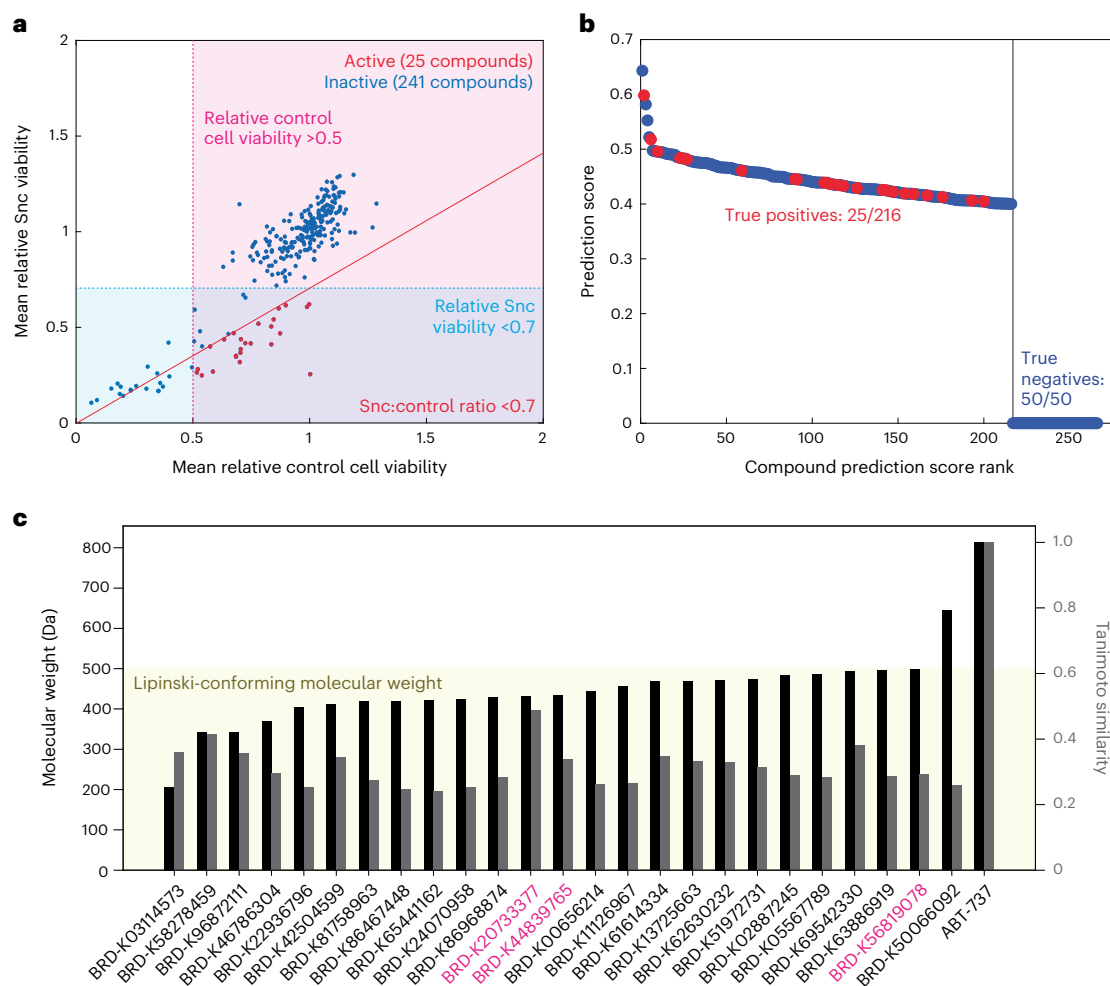
Fig. 2 | Identification of structurally diverse compounds with senolytic activity. a, Cell viability measurements for 266 curated compounds, including 216 high-ranking compounds from the Broad Institute's Drug Repurposing Hub or an extended Broad Institute library and the bottom-ranking 50 compounds from the Drug Repurposing Hub. Values indicate the mean of two biological replicates, and cell viability measurements are normalized with respect to the interquartile mean viability of each cell plate. The final concentration of all compounds was 10 μM. Sncs were treated with etoposide for senescence induction, and control cells were treated with vehicle (0.5% DMSO). **b**, Rank-ordered prediction scores of the 266 curated compounds, with high- and low-ranking compounds separated by the vertical line. Red points indicate curated compounds found to be active in **a. c**, Molecular weights and Tanimoto similarity scores of the 25 identified true positive compounds, rank-ordered by increasing molecular weight. For comparison, values for a known senolytic, ABT-737, are shown. Lipinski-conforming molecular weights are those <500 Da (yellow area), and lower Tanimoto similarity scores indicate higher structural novelty with respect to the training set. Three compounds on which we focus in this study are highlighted in magenta (see also Fig. 1g).

Drug Repurposing Hub[41] (with 5,819 unique compounds scored) and an extended Broad Institute library of 799,140 compounds. We found that the compounds exhibited a range of prediction scores, from 2.1×10^{-6} to 0.70 (Fig. 1f and Supplementary Data 2), suggesting that our model discriminates between predicted active and inactive compounds. Our model predictions were also structurally diverse, as indicated by visualizing the predicted compounds with t-distributed stochastic neighborhood embedding (t-SNE)[42]. Here, compounds corresponding to closer points are more structurally similar, and our plot revealed that the chemical spaces covered by high-ranking compounds from the Drug Repurposing Hub and the extended Broad Institute library are similar to, but extend beyond, that of active compounds from our screen (Fig. 1g). Furthermore, high-ranking compounds were largely separated from low-ranking compounds, indicating that our model demonstrates discriminatory ability.

We next narrowed our search space by applying filters selective for favorable medicinal chemistry properties and structural novelty (Extended Data Fig. 4 and Supplementary Data 3). First, we filtered compounds with promiscuously reactive substructures (pan-assay interference compounds, PAINS) and pharmacokinetically unfavorable substructures (Brenk substructures)[43,44]. Second, we aimed to curate compounds that were structurally distinct from known senolytics; we did so utilizing the Tanimoto similarity, a set-based measure of similarity that has a value of 1 when two compounds are identical and a value of 0 if two compounds have no substructure in common. Of our remaining compounds, we retained only those with low Tanimoto similarity (≤0.5) to any compound in our training dataset. From the filtered compounds, we curated all 10 compounds with prediction scores >0.4 from the Drug Repurposing Hub, and 206 in-stock compounds with prediction scores >0.4 from the extended Broad Institute library. As a negative control, we curated the bottom-ranking 50 filtered compounds, with prediction scores $<7 \times 10^{-5}$, from the Drug Repurposing Hub (Supplementary Data 3).

Measuring senolytic activity as before, our preliminary screens revealed that 25 of the 216 curated high-ranking compounds were active, in contrast to none of the 50 curated low-ranking compounds (Fig. 2a,b). The working hit rate (positive predictive value) of our approach was 11.6%, suggesting that our platform enriched for active

compounds relative to our initial screen (1.9% baseline enrichment), and that improvements to the model may further increase prediction accuracy. The low false negative rate of our approach also suggests that our model can contribute to filtering out molecules that probably do not possess senolytic activity in high-throughput screens. Notably, nearly all validated hits possessed Lipinski-conforming[45] molecular weights of <500 Da and were structurally dissimilar to all molecules in the training set, with Tanimoto similarity scores between 0.24 and 0.49 (Fig. 2c). This indicated that the hit compounds were drug-like and structurally novel.

Validation of compounds in models of therapy-induced senescence

We studied in detail the dose–response of several compounds that were particularly selective at 10 µM: of these, three compounds, BRD-K20733377, BRD-K56819078 and BRD-K44839765, exhibited encouraging therapeutic indices of 8.3, 12.0 and 4.7, respectively, which were at least comparable to the therapeutic index of ABT-737 (7.5; Fig. 3a–e and Extended Data Fig. 5). Given ABT-737's considerable selectivity and role in informing the discovery of other compounds with senolytic activity, including ABT-263, we focused on comparing the three identified compounds to ABT-737. Importantly, measurements of cellular viability across time indicate that all three compounds could selectively kill Sncs without inhibiting the growth of control cells at selective concentrations, in contrast to ABT-737 (Fig. 3f). Cellular viabilities of control, nonsenescent cells were increased after 3 days of incubation with 1% DMSO as a vehicle, demonstrating proliferation of control cells; in contrast, viabilities of etoposide-treated Sncs were decreased, an effect that could arise from post-treatment etoposide lethality on the timescale of our experiments[46,47]. Nevertheless, as compared to DMSO-treated Sncs and control cells, treatment with BRD-K20733377, BRD-K56819078 and BRD-K44839765 at concentrations between 1.5 and 3 µM resulted in the selective elimination of Sncs and no difference in the viabilities of control cells. In contrast, treatment with ABT-737 resulted in decreases in the viabilities of control cells, by ~20 to 50%, at concentrations including 0.2 and 1.5 µM (Fig. 3f).

Given that the identified compounds may exhibit more promising selectivity than ABT-737, we investigated their structural and physicochemical properties in greater detail. All three compounds are drug-like compounds from the extended Broad Institute library with no current clinical use. BRD-K56819078 and BRD-K44839765 share a benzothiazole-containing substructure, and all three compounds occupy a chemical space distinct from that of the training dataset, with the closest compounds being sulfadiazine, 3,4-dimethyoxybenzoic acid and salicylanilide, as measured by Tanimoto similarity (Figs. 1g and 2c, and Extended Data Fig. 6). Importantly, all three compounds are Lipinski-conforming and possess seven to ten rotatable bonds and topological polar surface areas between 109 and 143 Å² (Table 1 and Supplementary Data 4). These chemical properties suggest that BRD-K20733377 and BRD-K44839765 can be orally bioavailable, as they satisfy the Veber criteria of ≤10 rotatable bonds and topological polar surface area of ≤140 Å² (ref. 48). Additionally, the 143 Å² topological polar surface area of BRD-K56819078 is only slightly larger than the 140 Å² threshold[48]. In contrast, ABT-737 possesses a molecular weight of 879.5 Da, 17 rotatable bonds and a topological polar surface area of 164 Å². Low oral bioavailability, as well as undesirable side effects, has indeed limited the clinical application of ABT-737.

To further investigate the senolytic activities of BRD-K20733377, BRD-K56819078 and BRD-K44839765, we verified that these compounds were similarly selective against Sncs in an IMR-90 model of therapy-induced senescence using doxorubicin (Extended Data Fig. 7). SA-β-gal staining and quantification of p16, p21 and KI67 mRNA levels revealed that doxorubicin-treated wells exhibited a senescence phenotype similar to that of etoposide-treated cells, and all three compounds were indeed selective against doxorubicin-treated cells,

with therapeutic indices between 4.3 and 7.3 and IC$_{50}$ values ≤12.1 µM (Extended Data Fig. 7). Furthermore, IC$_{50}$ values for all three compounds were ≥20 µM for human embryonic kidney (HEK293) and liver carcinoma (HepG2) cells (Table 1), suggesting that all three compounds may not be strongly nephrotoxic or hepatotoxic at concentrations that are selective against Sncs, and that the compounds might target pathways specifically involved in cellular senescence.
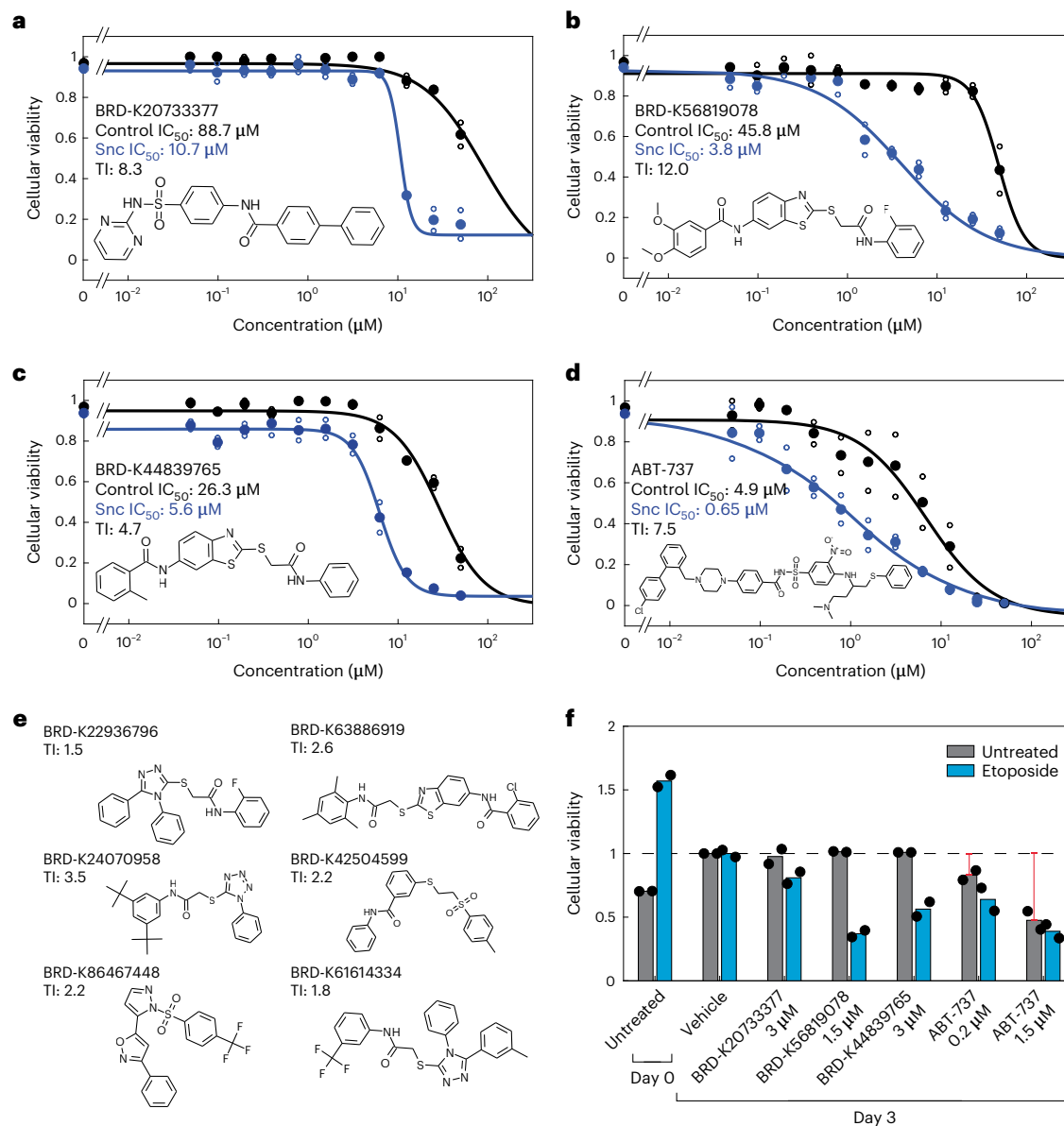
Validation of compounds in a model of replicative senescence

Orthogonal to our models of therapy-induced senescence, we measured the efficacy of BRD-K20733377, BRD-K56819078 and BRD-K44839765 in a model of replicative senescence. We cultured early- and late-passage IMR-90 cells, and late-passage cells were passaged until they became nondividing. To confirm senescence of late-passage cells, we performed SA-β-gal staining (Fig. 4a) and quantitation of p16, p21 and KI67 mRNA levels (Fig. 4b) as before; this revealed substantive SA-β-gal staining in late-passage cells and similarly increased or decreased p16, p21 and KI67 mRNA levels relative to those in the etoposide model. Treating early- and late-passage cells with each compound, we found that all three compounds were selective against late-passage Sncs (Fig. 4c–f). BRD-K20733377 and BRD-K56819078 were similarly selective against late-passage Sncs than ABT-737, while BRD-K44839765 was less—largely consistent with our findings for etoposide-treated Sncs (Fig. 3a–d). Intriguingly, the IC$_{50}$ values of all compounds were generally increased in early-passage cells as compared to vehicle-treated controls in the etoposide model, and in late-passage cells as compared to etoposide-treated Sncs. It is possible that these differences in IC$_{50}$ values might arise from continued post-treatment etoposide lethality[46,47] and increases in cellular permeability arising from DMSO treatment in the etoposide model, in addition to technical variability between experiments. Despite differences in IC$_{50}$ values, these findings consistently support the selectivity of the identified compounds in a model of replicative senescence.

Molecular docking and TR-FRET study of identified compounds

Given that BRD-K20733377, BRD-K56819078 and BRD-K44839765 are selective against Sncs in different models of senescence, we hypothesized that they may act on targets conserved in senescence pathways. We reasoned that a starting point for determining their potential mechanisms of action was to focus on known senolytic protein targets[49], including Bcl-2 and Bcl-2 family proteins, heat shock proteins such as Hsp90, and proteins involved in cell cycle regulation such as MDM2 and PI3K (Fig. 5a). Bcl-2 and Bcl-2 family proteins, including Bcl-XL, regulate cell death by apoptosis and are selectively inhibited by several senolytics, including ABT-737, ABT-263 and A-1331852 (refs. 10,12–15,50,51). Hsp90 is a ubiquitously expressed chaperone and stress response protein that stabilizes various client proteins, including those involved in oncogenesis and apoptosis, of which Akt aids in preventing apoptosis in Sncs[6,52,53]. Hsp90 inhibitors, including geldanamycin and 17-DMAG, have been identified as effective senolytics[6,53]. MDM2 directly binds to the transactivation domain of p53 and inhibits its transcriptional activity, an interaction that also results in the ubiquitination and proteomic degradation of p53, and senolytics including nutlin-3a and UBX0101 bind MDM2, inhibit the MDM2–p53 interaction and increase the availability of pro-apoptotic p53 (refs. 54–57). PI3K activation phosphorylates and activates Akt, which, as mentioned above, prevents apoptosis in Sncs, and senolytics including fisetin and quercetin bind PI3K (refs. 58–61).

Building on the above knowledge of senolytic protein targets, we performed molecular docking simulations to predict likely protein targets of BRD-K20733377, BRD-K56819078 and BRD-K44839765 (Fig. 5b). Here, as controls, we included known ligands of Bcl-2, Bcl-XL, Hsp90, MDM2 and PI3K (Fig. 5a), and we simulated the binding of each molecule to each of these proteins with a widely used molecular docking

Fig. 3 | Validation of identified compounds in a model of therapy-induced senescence. a–d, Dose–response curves of control and etoposide-treated IMR-90 cells treated with BRD-K20733377 (**a**), BRD-K56819078 (**b**), BRD-K44839765 (**c**) and ABT-737 (**d**) for comparison. Compounds were serially diluted twofold starting from a final concentration of 50 μM, and 0 μM (1% DMSO vehicle) treatment was included. Cells were treated for 3 days. Cellular viability was determined by the metabolic reduction of resazurin into fluorescent resorufin, and values are normalized by the fluorescence intensities of the average of two untreated samples from the same phenotype: here, a cellular viability of 1 indicates that of either untreated control cells or Sncs. Vehicle treatment may result in cellular viability values <1 due to effects of DMSO on cellular viability. Black curves indicate control (vehicle-treated) cells, and blue curves indicate (etoposide-treated) Sncs. Measurements are shown for two biological replicates in each treatment group (open points), and mean viability

values (closed points) were fitted to calculate IC_{50} values. The therapeutic index (TI) is the ratio of IC_{50} values for vehicle- and etoposide-treated cells. The chemical structure of each compound is shown in the inset of each plot. **e**, Additional structurally diverse active compounds, with the therapeutic index (TI) of each compound indicated for vehicle- and etoposide-treated cells (see also Extended Data Fig. 5). **f**, Cellular viability measurements for control (untreated) and etoposide-treated IMR-90 cells treated with varying concentrations of BRD-K20733377, BRD-K56819078, BRD-K44839765 and ABT-737. Cells were treated for 3 days. Values shown are normalized to the mean cell viability value for cells treated with vehicle (1% DMSO) for 3 days, such that cell proliferation in the presence of DMSO vehicle between days 0 and 3 is indicated by an increase in cellular viability values. Data from two biological replicates are shown (black points), and bars represent average values. Red lines highlight inhibited control cell proliferation induced by treatment with ABT-737.

platform, AutoDock Vina[62]. We obtained the protein structure of each target from a corresponding complex with a bound inhibitor from the Protein Data Bank (PDB)[63–67], and we defined the active site of each protein structure on the basis of the conformation of the corresponding bound inhibitor. Representing each chemical compound in three dimensions, docking each compound into the active site of each structure resulted in a range of predicted binding affinity values (Fig. 5c).

Notably, taking the protein–ligand interaction with the lowest binding affinity (highest activity) to be the most likely—of the targets studied—for any given compound, our approach accurately predicted the known binding interactions of ABT-737 to Bcl-2, geldanamycin to Hsp90, and fisetin to PI3K (Fig. 5c). Illustrating the potential limitations of our approach, nutlin-3a was predicted to bind Bcl-2 with lower affinity than that of its known primary target, MDM2 (ref. 66). Intriguingly, however,

Table 1 | Physicochemical properties and cytotoxicity of identified compounds

Compound	BRD-K20733377	BRD-K56819078	BRD-K44839765	ABT-737
Canonical SMILES string	C1=CC=C(C=C1)C2=CC=C(C=C2)C(=O)NC3=CC=C(C=C3)S(=O)(=O)NC4=NC=CC=N4	COC1=C(C=C(C=C1)C(=O)NC2=CC3=C(C=C2)N=C(S3)SCC(=O)NC4=CC=CC=C4F)OC	CC1=CC=CC=C1C(=O)NC2=CC3=C(C=C2)N=C(S3)SCC(=O)NC4=CC=CC=C4	CN(C)CCC(CSC1=CC=CC=C1)NC2=C(C=C(C=C2)S(=O)(=O)NC(=O)C3=CC=C(C=C3)N4CCN(CC4)CC5=CC=CC=C5C6=CC=C(C=C6)Cl)[N+](=O)[O-]
Molecular weight	430.48 Da	497.56 Da	433.55 Da	813.43 Da
Number of heavy atoms	31	34	30	56
Number of rotatable bonds	7	10	8	17
Topological polar surface area (TPSA)	109.43 Å^2	143.09 Å^2	124.63 Å^2	164.49 Å^2
Lipinski-conforming	Yes	Yes	Yes	No; MW >500 Da g mo^{l-1}, TPSA >140 Å^2
Veber-conforming	Yes	No; TPSA >140 Å^2	Yes	No; number of rotatable bonds >10, TPSA >140 Å^2
PAINS	None	None	None	None
Brenk substructures	None	None	None	Yes; nitro group and oxygen–nitrogen single bond
HEK293 IC$_{50}$	51.1 μM	21.4 μM	159.5 μM	28.8 μM
HepG2 IC$_{50}$	70.3 μM	420.7 μM	382.6 μM	131.9 μM

For comparison, values for ABT-737 are shown. Lipinski-conforming indicates that a compound violates no more than one of Lipinski's rule of five: (a) ≤5 hydrogen bond donors, (b) ≤10 hydrogen-bond acceptors, (c) molecular weight <500 Da and (d) log P partition coefficient <5. Veber-conforming indicates that a compound violates none of Veber's rules for oral bioavailability: (a) ≤10 rotatable bonds and (b) TPSA ≤140 Å^2. IC$_{50}$ values for human embryonic kidney (HEK293) and human liver carcinoma (HepG2) cells represent values inferred from curve-fitting with data from two biological replicates, as detailed in Methods.

nutlin-3a has also been evidenced in previous work to bind Bcl-2 family proteins, including Bcl-2 and Bcl-XL, suggesting that nutlin-3a may be promiscuous[68]. On the basis of these supportive preliminary results, we investigated in detail the docking predictions for BRD-K20733377, BRD-K56819078 and BRD-K44839765, which predicted that all three compounds most likely bind Bcl-2 with binding affinities comparable to those of the geldanamycin-Hsp90 and nutlin-3a-Bcl-2 interactions (Fig. 5c). To further interpret each predicted binding interaction, we visualized the docked pose of each compound in comparison to that of ABT-737 (Fig. 5d). Examination of each binding pose suggested that the three identified compounds could, like ABT-737, interact with residues in common binding pockets of Bcl-2, including those containing L97, A100, G145 and A149 (Fig. 5d).

To summarize, our molecular docking simulations suggested that BRD-K20733377, BRD-K56819078 and BRD-K44839765 most likely bind Bcl-2, and that this binding may involve similar residues or binding pockets as those of ABT-737. We directly tested this hypothesis using a TR-FRET assay, in which Bcl-2 binding activity to a peptide ligand specific to its active site is measured. We found that all three compounds indeed inhibited Bcl-2, and this inhibition occurs at micromolar concentrations comparable to the corresponding Snc IC$_{50}$ values in the therapy-induced and replicative senescence models (Fig. 5e). Intriguingly, ABT-737 appears to be a more potent inhibitor of Bcl-2 than the three compounds, an observation consistent with ABT-737's lower IC$_{50}$ value against Sncs (Figs. 3a–d and 4c–f, and Extended Data Fig. 7). Taken together, these results support the hypothesis that BRD-K20733377, BRD-K56819078 and BRD-K44839765 selectively target Sncs in part by inhibiting Bcl-2.

Initial toxicity profiling of identified compounds

As BRD-K20733377, BRD-K56819078 and BRD-K44839765 exhibit promising senolytic activities and physicochemical properties, we further assessed their toxicity profiles. Diverse toxicological assays, including those examining cardiotoxicity, neurotoxicity and mitochondrial toxicity, are needed to comprehensively evaluate the safety profiles of lead compounds and inform subsequent in vivo experiments and the possibility of side effects; for our preliminary studies, we focused

on mechanistic toxicity, as surveyed by hemolysis, and genotoxicity, as assessed by mutagenic potential. Hemolysis is often a severe toxic liability of systemically-administered compounds that kill cells, and hemolytic activity may preclude the use of compounds for injection, a route of administration commonly used for senolytics in addition to oral[69–71]. Measuring the release of hemoglobin from human red blood cells extracted from whole blood, we found that treatment with all three compounds, in addition to ABT-737, did not induce substantial hemolysis up to a final concentration of 100 μM—approximately 10× the corresponding therapeutic concentrations in the therapy-induced and replicative senescence models (Extended Data Fig. 8). In contrast, treatment with Triton X-100, a detergent with hemolytic activity, resulted in substantial hemolysis at concentrations ≥0.01% (w/w). Furthermore, we assessed potential genotoxic effects using a bacterial Ames test, in which the number of bacterial revertants from a base-pair substitution is measured after compound treatment to assess mutagenic potential. In contrast to treatment with ~1 μM 4-nitroquinoline 1-oxide, a potent mutagen, treatment with all three compounds at 100 μM, in addition to ABT-737, did not induce substantial reversion of bacterial cultures (Extended Data Fig. 8). These preliminary findings suggest that the identified compounds may possess favorable toxicity profiles, underscoring their potential for further development.

In vivo efficacy of BRD-K56819078 in an aged mouse model

Given the favorable selectivity and toxicity profiles of BRD-K20733377, BRD-K56819078 and BRD-K44839765, we selected BRD-K56819078, one of the more selective of the three compounds across all senescence models (Figs. 3a–d and 4c–f, and Extended Data Fig. 7), for in vivo testing. Previous measurements of Sncs in animal models have focused on Snc accumulation in the kidneys[72], which has been suggested to exhibit more salient increases in senescence-associated biomarkers than in other tissues in humans[73]. As a baseline experiment, we collected the kidneys of naïve young and aged C57BL/6J mice and measured SA-β-gal staining and p16 and p21 mRNA expression (Fig. 6a). We found that the SA-β-gal-positive area in different images of young mouse kidneys were, on average, ~40% less than that of aged mouse kidneys (Fig. 6b).
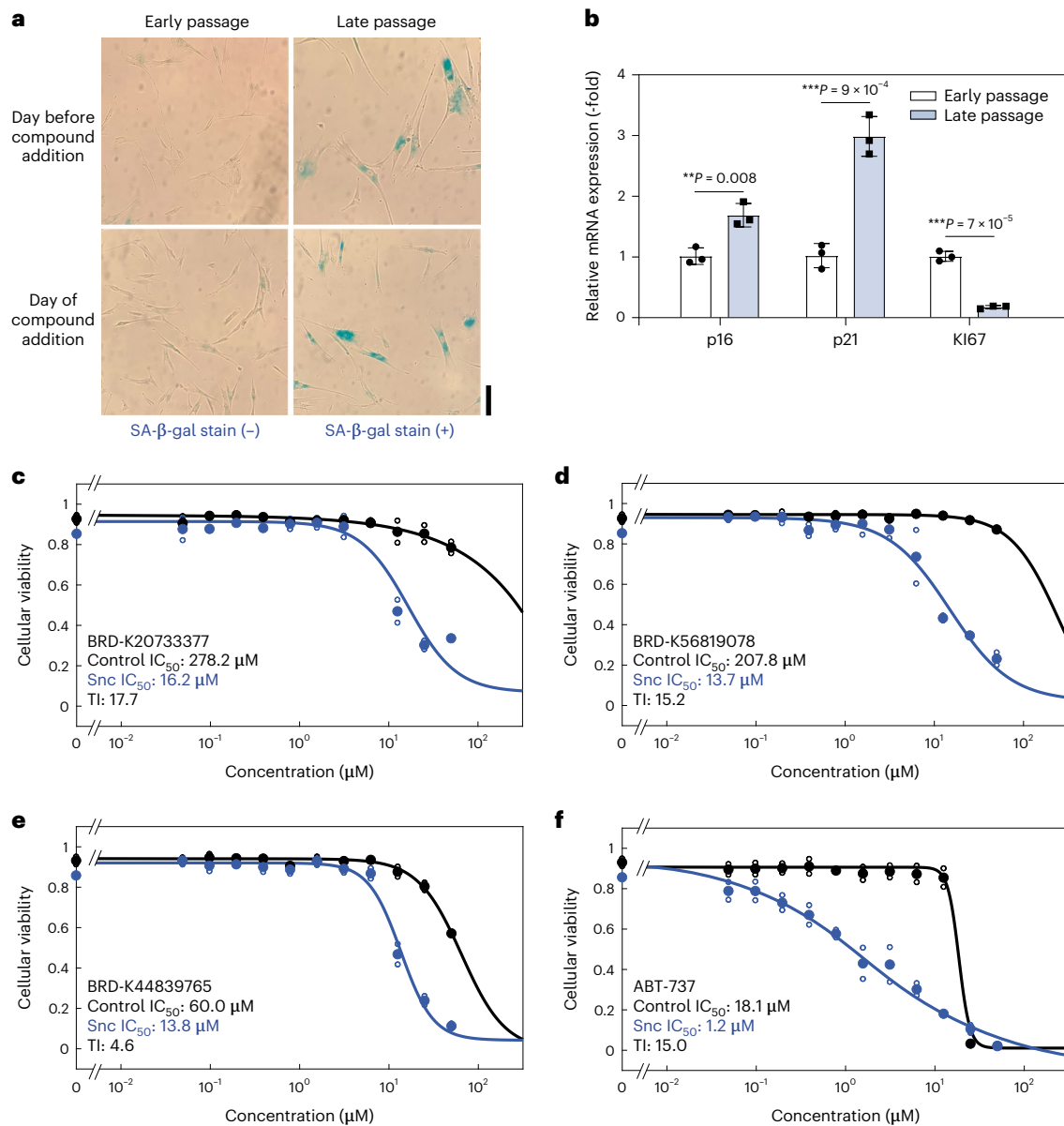
**Fig. 4 | Validation of identified compounds in a model of replicative senescence. a**, SA-β-gal staining of early- and late-passage IMR-90 cells plated at times corresponding to the day before and day of compound addition. Each image is representative of two biological replicates. Scale bar, 100 μm. **b**, Relative mRNA expression of p16, p21 and KI67 in early- and late-passage IMR-90 cells collected on the day of compound addition. Data from three biological replicates are shown (black points), and bars represent average values. Error bars indicate one standard deviation. Two-sided two-sample *t*-test for differences in mean value: **$P < 0.01$, ***$P < 0.005$. **c–f**, Dose–response curves of early- and late-passage IMR-90 cells treated with BRD-K20733377 (**c**), BRD-K56819078 (**d**), BRD-K44839765 (**e**) and ABT-737 (**f**) for comparison. Compounds were serially diluted twofold starting from a final concentration of 50 μM, and 0 μM (1%

DMSO vehicle) treatment was included. Cells were treated for 3 days. Cellular viability was determined by the metabolic reduction of resazurin into fluorescent resorufin, and values are normalized by the fluorescence intensities of the average of two untreated samples from the same phenotype: here, a cellular viability of 1 indicates that of either untreated early- or late-passage cells. Vehicle treatment may result in cellular viability values <1 due to minor effects of DMSO on cellular viability. Black curves indicate control (early-passage) cells, and blue curves indicate (late-passage) Sncs. Measurements are shown for two biological replicates in each treatment group (open points), and mean viability (closed points) were fitted to calculate IC_{50} values. The therapeutic index (TI) is the ratio of IC_{50} values for early- and late-passage cells.

Consistent with a decrease in senescent cell burden, average mRNA expression of p16 and p21 were decreased by >90% and ~30%, respectively, in young mice relative to aged mice (Fig. 6c). These findings indicate that differences in mouse age, and hence the accumulation of Sncs, are reflected in senescence-associated biomarkers in the kidneys.

Building on the foregoing results, we treated aged C57BL/6J mice with vehicle (10% DMSO:45% PEG300:45% water for injection w/w) or BRD-K56819078 (intraperitoneally at 25 mg kg⁻¹ per injection) on days 0, 2, 4, 7, 9 and 11 of a 14 day experiment (Fig. 6d). Notably,

BRD-K56819078 was well tolerated by all treated mice and did not result in obvious toxicity, abnormal behavior or abnormal decreases in weight. We collected the kidneys of all mice on day 14 and measured SA-β-gal staining and p16 and p21 mRNA expression. This revealed significant decreases in the SA-β-gal-positive areas of mice treated with BRD-K56819078, with average decreases of ~20% relative to vehicle-treated mice (Fig. 6e). mRNA expression of p16 and p21 was significantly decreased in mice treated with BRD-K56819078, with average decreases of ~60% and ~30%, respectively, in mice treated with BRD-K56819078
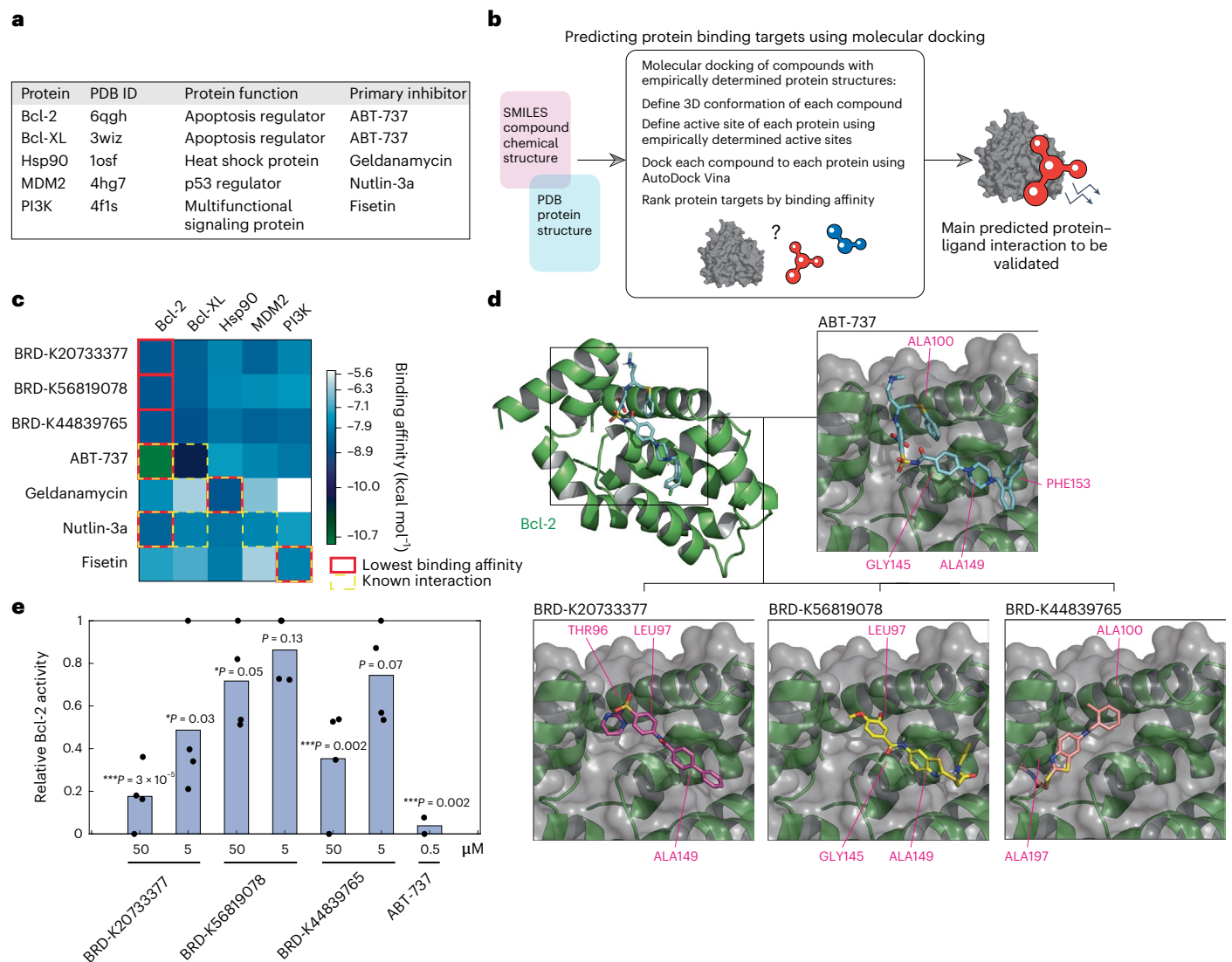
Fig. 5 | Molecular docking- and TR-FRET-based identification of Bcl-2 as a potential binding target. a, Known senolytic protein targets in humans. PDB identifiers used for molecular docking and relevant protein functions are indicated. As controls for the docking simulations, examples of known binding inhibitors of each protein were identified, and their molecular structures were used for docking. **b**, Schematic of the molecular docking approach. Experimentally determined protein structures in complex with various inhibitors were curated from the PDB, and protein active sites were determined from the inhibitor-bound conformations. Chemical compounds of interest were represented in three dimensions (3D) and docked in the active site of each protein structure using AutoDock Vina. Binding affinities were then calculated for each protein–ligand pair and used to rank likely binding targets (in **c**). **c**, Predicted binding affinities (kcal mol⁻¹) for each of the three identified compounds and known inhibitor compounds with each of the known senolytic protein targets in **a**. Values are from docking simulations involving each potential protein–ligand pair and are representative of 32 runs each. Lower binding affinity values indicate higher predicted binding activity. For each ligand, the protein target with the lowest predicted binding affinity of those tested is highlighted in red. Known protein–ligand interactions are highlighted in yellow (dashed lines). **d**, Molecular docking poses of ABT-737 (positive control; main figure and inset), BRD-K20733377 (inset), BRD-K56819078 (inset) and BRD-K44839765 (inset) with Bcl-2. Amino acid residues are indicated in magenta. Compound structures are colored by atom type (noncarbon atoms) or arbitrarily (carbon atoms) for color contrast. **e**, Relative Bcl-2 activity in the presence of varying concentrations of BRD-K20733377, BRD-K56819078, BRD-K44839765 and ABT-737, as measured by TR-FRET. Black points indicate values from individual biological replicates, and blue bars indicate average values. Unpaired two-sided t-tests for no change in Bcl-2 activity after compound treatment (compared to relative Bcl-2 activity values of 1 arising from vehicle treatment only): *$P \leq 0.05$, ***$P < 0.005$.

relative to vehicle-treated mice (Fig. 6f). Taken together, these in vivo experiments indicate that BRD-K56819078 significantly decreased senescent cell burden and mRNA expression of senescence-associated genes in the kidneys, suggesting the promise of BRD-K56819078 and other compounds for further development.

Discussion

In this study, we trained deep learning models with the results of a small molecule screen for senolytic activity and applied our models to discover structurally diverse compounds with senolytic activity from a chemical space of >800,000 compounds (Fig. 1). Our approach augments high-throughput screens for compounds with senolytic activity—leading to a sixfold increase in the working hit rate (positive predictive value)—and we anticipate that increasing the number of active compounds used in model training could further increase prediction accuracy (Fig. 2). Detailed studies of three senolytic compounds with favorable medicinal chemistry properties indicate that they are selective against Sncs in models of therapy-induced and replicative senescence (Figs. 3 and 4).
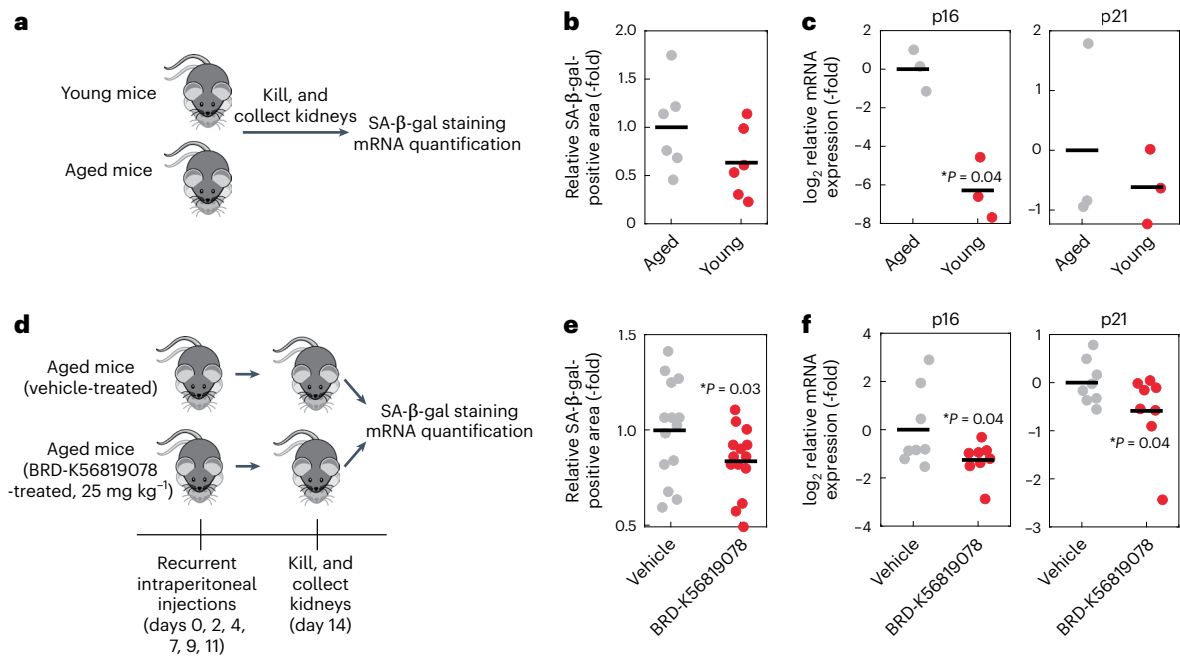
Fig. 6 | In vivo efficacy of BRD-K56819078 in an aged mouse model.
a, Schematic of the validation experiment. Kidneys were collected from naïve young and aged mice and tested for senescent cell burden, as measured by SA-β-gal staining and mRNA expression of p16 and p21. **b**, Relative SA-β-gal-positive area in kidney sections of young and aged mice (*n* = 3 mice each, and one kidney per mouse). Data shown are from two fields of view for each kidney, and horizontal lines represent average values. **c**, Relative mRNA expression of p16 and p21 in the kidneys of young and aged mice (*n* = 3 mice each, and one kidney per mouse). Horizontal lines represent average values. One-sided, two-sample permutation test for differences in mean value: **P* ≤ 0.05. **d**, Schematic of the aged mouse experiment. Kidneys were collected from aged mice treated

intraperitoneally six times with vehicle or BRD-K56819078 (25 mg kg⁻¹ per injection) and tested for senescent cell burden, as measured by SA-β-gal staining and mRNA expression of p16 and p21. **e**, Relative SA-β-gal-positive area in kidney sections of vehicle- and BRD-K56819078-treated aged mice (*n* = 7 mice each, and one kidney per mouse). Data shown are from two fields of view for each kidney, and horizontal lines represent average values. One-sided, two-sample permutation test for differences in mean value: **P* ≤ 0.05. **f**, Relative mRNA expression of p16 and p21 in the kidneys of vehicle- and BRD-K56819078-treated aged mice (*n* = 8 mice each, and one kidney per mouse). Horizontal lines represent average values. One-sided, two-sample permutation test for differences in mean value: **P* ≤ 0.05.

To study potential mechanisms of action, we developed a molecular docking-based approach to predict the interactions of these compounds with known senolytic protein targets. Our results suggest that the compounds selectively target Sncs in part by inhibiting Bcl-2, a hypothesis supported by empirical TR-FRET measurements (Fig. 5). Moreover, we tested one compound, BRD-K56819078, in aged mice and found that it significantly decreased senescent cell burden and mRNA expression of senescence-associated genes in the kidneys (Fig. 6). Taken together, these findings demonstrate that combining experiment with computation and deep learning can enable one to efficiently discover senolytic compounds and rapidly elucidate their potential mechanisms of action. It is important to highlight that we anticipate this approach to facilitate lead generation: in addition to optimizing compounds for selectivity, additional studies should further determine the in vivo efficacy, absorption, distribution, metabolism and excretion (ADME) properties, and potential side effects of lead compounds in order to assess their clinical suitability. These are lines of additional research that our preliminary toxicity profiling results (Extended Data Fig. 8) and in vivo experiments (Fig. 6) only begin to address.

While our deep learning approach is promising, it also has limitations. First, machine learning approaches are generally limited by the training data used. Although our screen of 2,352 compounds and activity criteria resulted in enough active compounds to train models with predictive power, more structural diversity in the training set will allow models to more accurately infer the chemical substructures that confer senolytic activity. This will help to facilitate the identification of more structurally diverse senolytics. Datasets containing multidimensional readouts of senescence-associated markers, in addition to

cellular viability for different cell lines and compound concentrations, may improve the predictive capabilities of these models. Second, our approach relies on training data generated from phenotypic screens to make predictions of senolytic activity. Mechanistically elucidating compound binding targets remains a challenge, despite elegant studies that have aimed to address this problem[25–27,74–76], in part because of the need for detailed predictions and their experimental validation. Our results suggest that canonical molecular docking simulations can discriminate between known binders and nonbinders of senolytic protein targets; yet, docking is also known to produce false positives[77–79], and predictions arising from docking should be empirically validated to determine accuracy. Community efforts that build on the recent bioinformatics and cheminformatics literature to combine novel, and potentially explainable[80], machine learning approaches with additional experimental data may help to address both these limitations.

Moving forward, we believe that the emerging field of senolytics is well positioned to benefit from machine learning-based approaches that rely on phenotypic information. Senolytics have been thought to be more similar to antibiotics than any other type of drug: they aim to target and eliminate a cellular phenotype as opposed to a specific receptor, enzyme or biochemical pathway[16]. Indeed, the phenotypic and network-based approaches used to discover and model the effects of senolytics have had more in common with those used for antibiotics than typical one-target–one-drug–one-disease approaches[16,81]. In addition to further exploring chemical space, we anticipate that future work will leverage explainable machine learning approaches[80] and detailed mechanism of action information to help elucidate the biological principles, phenotypes and networks underlying how senolytics selectively target Sncs. Together, these approaches will enable the

efficient discovery of novel senolytic compounds and their biological targets, contributing to our evolving understanding of senolytics and facilitating their development as a class of therapeutics.

Methods

This study complies with all relevant ethical regulations; in particular, the experiment described below in 'Aged mouse model experiments' was performed in accordance with protocol IS00000852-6, approved by Harvard Medical School Institutional Animal Care and Use Committee and the Committee on Microbiological Safety.

Cell culture

Human lung fibroblast (IMR-90) cells were obtained from the American Type Culture Collection (ATCC, CCL-186) and passaged less than ten times (less than 30 population doublings) for all experiments, with the exception of high-passage cells used in the model of replicative senescence (see 'Replicative senescence' below). Cells were cultured in growth media comprising Eagle's minimum essential medium (ATCC 30-2003) supplemented with 10% fetal bovine serum (Thermo Fisher 16140071) and 1% penicillin–streptomycin (Thermo Fisher 15070063). Cells were incubated in a humidity-controlled incubator at 37 °C with 5% CO_2. Cells were detached using trypsin–EDTA (0.05%; Gibco 25300120).

Etoposide-induced senescence

IMR-90 cells were cultured as described above. At between 30% and 50% confluence, the medium was replaced with complete growth medium containing vehicle (0.5% DMSO, MilliporeSigma D5879) or complete growth medium containing 50 µM etoposide (prepared as a 1:200 dilution of a 10 mM stock solution in DMSO; etoposide, MilliporeSigma E1383). Cells were treated for 2 days, after which the medium was replaced with fresh growth medium and cells were allowed to recover for 4 days. Cells were then plated as described below.

Doxorubicin-induced senescence

As an additional model of therapy-induced senescence, we used a model of doxorubicin-induced senescence. IMR-90 cells were cultured as described above. At between 30% and 50% confluence, the medium was replaced with complete growth medium containing vehicle (0.5% DMSO) or complete growth medium containing 0.5 µM doxorubicin (prepared as a 1:200 dilution of a 0.1 mM stock solution in DMSO; doxorubicin, Cayman Chemical 15007). Cells were treated for 2 days, after which the medium was replaced with fresh growth media and cells were allowed to recover for 4 days. Cells were then plated as described below.

Replicative senescence

As an orthogonal model of cellular senescence, we used a model of replicative senescence. Early-passage IMR-90 cells (passage number <3, corresponding to less than 9 population doublings from supplier's stock) were used. High-passage IMR-90 cells were cultured as described above and passaged until cells became nondividing (passage number >10, corresponding to at least 30 population doublings from supplier's stock). Senescence was confirmed with SA-β-gal staining and mRNA quantification, as described in the main text. Cells were then plated as described below.

SA-β-gal staining

On each of two days before or on the day of compound addition—corresponding to days 0 and 1 shown in Extended Data Fig. 1—cells treated with vehicle, etoposide or doxorubicin (models of therapy-induced senescence) or early-passage and late-passage cells (model of replicative senescence) were plated onto six-well plates at an initial density of $0.2–0.5 \times 10^6$ cells per well. Cells were then incubated overnight for adhesion. The following day, SA-β-gal staining was performed using a commercial staining kit (Cell Signaling Technology 9860) following the manufacturer's instructions. Briefly, cells in each well were rinsed

once with 2 ml of Dulbecco's phosphate-buffered saline (DPBS; VWR 02-0119-0500). Cells in each well were fixed for 15 min at room temperature using 1 ml of 1× fixative solution. Next, cells in each well were rinsed twice with DPBS, then 1 ml of β-galactosidase staining solution (pH 6.0) was added. Plates were sealed with parafilm and incubated overnight at 37 °C in a dry incubator. The next day, cells in each well were imaged with a light microscope to detect staining, as shown in Figs. 1b and 4a and Extended Data Fig. 7.

mRNA quantification using quantitative PCR

Total RNA was extracted using an RNeasy mini kit from Qiagen (Qiagen 74104) following the manufacturer's instructions. For qPCR analysis, complementary DNAs were synthesized using a QuantiTect Reverse Transcription Kit from Qiagen following the manufacturer's instructions (Qiagen 205311). Real-time PCR amplifications were performed in 96-well optical reaction plates using a Power SYBR Green PCR Master Mix from Thermo Fisher (Thermo Fisher 4368577). The following primers were used, and the relative expression of each gene was determined by normalization to GAPDH expression for each sample:

p16 forward primer: CCCAACGCACCGAATAGTTA
p16 reverse primer: ACCAGCGTGTCCAGGAAG
p21 forward primer: TGTCCGTCAGAACCCATGC
p21 reverse primer: AAAGTCGAAGTTCCATCGCTC
KI67 forward primer: GAGGTGTGCAGAAAATCCAAA
KI67 reverse primer: CTGTCCCTATGACTTCTGGTTGT
GAPDH forward primer: GGAGCGAGATCCCTCCAAAAT
GAPDH reverse primer: GGCTGTTGTCATACTTCTCATGG

Relative expression values for each of p16, p21 and KI67 were then normalized to those of control (DMSO-treated or early passage) cells for comparison, as shown in Figs. 1c and 4b and Extended Data Fig. 7.

Chemical compounds for screens

The screening library is from MicroSource Discovery Systems and consists largely of US Food and Drug Administration-approved drugs, drugs currently in clinical trials, and natural products[23] (2,560 compounds total). We supplemented the screening library with 20 compounds, most of which have senolytic activity reported in the literature, and all of which were procured from commercial suppliers, as detailed in Supplementary Data 1. After deduplication of 228 compounds, we screened the 2,352 unique compounds for senolytic activity as described below. All compounds used in our screen can be found in Supplementary Data 1.

Chemical screening

For all screening experiments, 99 µl of cells were plated into each well of a 96-well clear flat-bottom, black polystyrene tissue-culture-treated plate (Corning 3904) at a density of ~10^4 cells per well. Plates were incubated overnight for adhesion. The day after plating, 1 µl of each compound, prepared as either a 1 mM stock solution in DMSO (10 µM final concentration screen) or 0.1 mM stock solution in DMSO (1 µM final concentration screen), was added to each well using an Agilent Bravo liquid handler. A built-in slow mixing step involving aspirating and dispensing was used to enhance distribution of the added compounds in solution. Cells were incubated for 3 days, after which resazurin (MilliporeSigma R7017) was added to each well to a final concentration of 0.15 mM. After an additional 1 day of incubation, the fluorescence excitation/emission at 550/590 nm was read using a SpectraMax M3 plate reader and manufacturer software (SoftMax Pro 6). Experiments were performed in biological duplicate.

For the validation dose–response measurements shown in Extended Data Fig. 2, threefold serial dilutions of compound were prepared in DMSO, then added to cell plates (final concentration of DMSO, 1%). Cell viability was then assayed as detailed above, and resazurin fluorescence values were linearly interpolated with respect to values from empty and positive control (nontreatment) wells.

Experiments were performed in biological duplicate each on two independent occasions. When possible, chemical stocks from commercial suppliers were used: econazole nitrate (Cayman Chemical 20223), artenimol (Cayman Chemical 19846) and ABT-263 (Cayman Chemical 11500) were from Cayman Chemical, and dehydrodeguelin was aliquoted from the screening library.

Calculation of cellular viability values in dose–response curves

To determine relative cell viability values for the dose–response curves shown in Figs. 3 and 4 and Extended Data Figs. 2, 5 and 7, resazurin fluorescence intensity measurements were measured after 3 days of compound treatment and 1 day of resazurin incubation. For each sample, the fluorescence intensity value was normalized by the mean of two untreated control values. Cellular viability values are therefore indicated as fractions of the cellular viability of untreated controls. Vehicle (1% DMSO) control values are included in each dose–response curve. Experiments were performed in biological duplicate each on two independent occasions.

Calculation of baseline cellular viability values

In Fig. 3f, cellular viability was calculated as above for untreated IMR-90 cells and etoposide-treated IMR-90 cells, which were treated with DMSO or compounds for 3 days and then incubated in the presence of resazurin for 1 day. Additionally, baseline cellular viability values were calculated for untreated cells at the start of the experiment. Resazurin was added to a final concentration of 0.15 mM on the day of seeding (corresponding to day 0 in Extended Data Fig. 1). Cells were incubated for 1 day, then fluorescence intensity values were read. These fluorescence intensity values were normalized by the mean of two vehicle (1% DMSO)-treated control values at day 3, such that cell proliferation between days 0 and 3 in the presence of DMSO vehicle is indicated by an increase in cellular viability values. Experiments were performed in biological duplicate on one independent occasion.

Curve-fitting and estimation of IC$_{50}$ values

To estimate IC$_{50}$ values in dose–response curves, we used nonlinear least-squares fitting (the lsqcurvefit function in MATLAB, ver. R2019b) to fit relative growth values to Hill functions of the form

$$H(x) = b_0 + \frac{mx^\beta}{x_{0.5}^\beta + x^\beta},$$

while enforcing $H \geq 0$ for all x. IC$_{50}$ values were determined by numerically solving the best-fit Hill function for x given $H(x) = 0.5$.

Deep learning model

The deep learning model used in this work builds on that applied in ref. 23 and uses Chemprop (https://github.com/chemprop/chemprop), a software package for molecular property prediction that implements the graph neural networks described below and in the main text. For each compound, a graph-based molecular representation was generated from the compound's simplified molecular-input line-entry system (SMILES) string using RDKit (ver. 2021.09.01). A feature vector for each atom and bond in the compound was generated on the basis of the following computable features:

1. atom features including the atomic number, number of bonds for each atom, formal charge, chirality, number of bonded hydrogen atoms, hybridization, aromaticity and atomic mass;
2. bond features including the bond type (single, double, triple or aromatic), conjugation, ring membership and stereochemistry.

The model implements the bond-based message-passing convolutional neural network described in ref. 34. Here, each message (a real number) associated with a bond is updated by summing the messages from neighboring bonds, concatenating the current bond's message with the sum, and applying a single neural network layer with a nonlinear activation function. After a fixed number of message-passing steps, the messages across the molecule are summed to produce a final message representing the molecule. This message is inputted into a feed-forward neural network, which outputs a final prediction of the compound's senolytic activity. The final output is a real number between 0 (is not senolytic) and 1 (is senolytic), describing the probability that the compound is predicted to be senolytic.

Model optimization

Following ref. 23, three model optimizations were used to improve model performance. First, 200 molecule-level features computed with RDKit, as summarized in Supplementary Data 1, were added to the graph-based representation of each compound. This step was performed to provide additional information about predicted global properties of each compound, augmenting the local message-passing approach. Second, we used Bayesian hyperparameter optimization in order to select hyperparameters for the model. Doing so using Chemprop's hyperopt function, we found and utilized the following hyperparameters for all Chemprop models: depth, 2; dropout, 0; number of feedforward layers, 3; hidden size, 600. Finally, we used ensembling to increase the robustness of Chemprop model predictions, as detailed separately for 'Model evaluation' and 'Model predictions and filtering' below.

Model evaluation

Each compound in our initial training dataset of 2,352 compounds was assigned a binary activity value of 0 (no senolytic activity) or 1 (possesses senolytic activity), as shown in Fig. 1d. To evaluate model performance using the auPRC, the initial training dataset was partitioned such that 80% of the compounds (1,882 compounds) were reserved for training and validation and 20% of compounds (470 compounds) were withheld for testing and calculation of PRCs. Active compounds in each group were distributed similarly as in the overall dataset (10 of 470 compounds, or 2.1%). For each Chemprop model, training was performed for 30 epochs using random 80–10–10 training–validation–testing splits of the training subset, with each model being assigned a different random seed. By default, and consistent with previous work[23], the binary cross entropy was used as the loss function. Ten models were then pooled together to form an ensemble. This ensemble of models was applied to the withheld testing subset, and prediction scores of the ensemble were taken as the average of the prediction scores of all ten models in the ensemble. Precision–recall curves were generated by comparing the prediction score to the withheld activity value for each compound in the testing subset using scikit-learn.

Random forest classifiers were independently trained using scikit-learn. The same training and withheld test sets as above were used, and an exhaustive hyperparameter grid search was performed. A total of 360 random forest models were trained for hyperparameters in the following combinatorial space: maximum depth between 5 and 40, in intervals of 5; number of estimators between 20 and 100, in intervals of 20; maximum features between 20 and 180, in intervals of 20. Precision–recall curves were generated using scikit-learn as above. For both our Chemprop and random forest models, bootstrapping with 100 subsamples, each subsample with size equal to the test set, was used to calculate 95% confidence intervals for the auPRC and bootstrapped variations of precision–recall curves (Fig. 1e and Extended Data Fig. 3).

t-SNE and visualization

For the t-SNE analysis shown in Fig. 1g, we used sklearn.manifold's TSNE function in conjunction with Morgan fingerprint representations of all compounds (radius 2 and number of bits 2,048) to visualize compounds. The Jaccard distance, which is another name for Tanimoto distance, was used as the distance metric; the Tanimoto distance is defined as

Tanimoto distance = 1 – Tanimoto similarity, and the Tanimoto similarity between two fingerprints is given by the quotient of the number of 1-bits in the intersection of both fingerprints divided by the number of 1-bits found in their union. All calculations of Tanimoto similarity used in this work are based on Morgan fingerprint representations of all compounds (radius 2 and number of bits 2,048). The choice of the Jaccard metric implies that the distance between points reflects the Tanimoto similarity of the corresponding compounds, with greater t-SNE distance corresponding to lower Tanimoto similarity[23]. A perplexity parameter of 10 was used to generate plots with well-spaced data points.

Model predictions and filtering
For the final model, 20 Chemprop models were each trained for 30 epochs using random 80–10–10 training–validation–testing splits. The models were then deployed to predict the senolytic activities of 804,959 compounds comprising the Broad Institute's Drug Repurposing Hub[41] (with 5,819 unique compounds scored) and an extended Broad Institute library of 799,140 compounds. For each compound, the prediction scores of all models were averaged to determine the final prediction score for the compound. All final prediction scores are provided in Supplementary Data 2. Following prediction of senolytic activity, compounds with high prediction scores (>0.4) possessing PAINS and Brenk substructures were filtered out using rdkit.Chem's FilterCatalog package. The remaining compounds with high prediction scores were filtered on the basis of the Tanimoto similarity, and all calculations of Tanimoto similarity were performed as described above.

Chemical curation
For initial screens of compounds with high or low predicted senolytic activity, most compounds were procured from the Broad Institute Center for the Development of Therapeutics. ABT-737 was from Cayman Chemical (Cayman Chemical 11501). For all other experiments, compounds were purchased commercially from ChemBridge and Maybridge. All catalog numbers are provided in Supplementary Data 3.

Calculation of physicochemical properties
For each compound, the physicochemical properties presented in Table 1 and Supplementary Data 4 were calculated from the corresponding SMILES string using SwissADME[82].

Measuring cytotoxicity against HepG2 and HEK293 cells
Cytotoxicity in human embryonic kidney (HEK293) and liver carcinoma (HepG2) cells was assayed as above using a resazurin assay. Cells were obtained from ATCC (ATCC CRL-1573 and HB-8065), passaged <10 times and grown in Dulbecco's modified Eagle's Medium (Corning 10-013-CV) supplemented with 10% fetal bovine serum and 1% penicillin–streptomycin. Then, 99 μl of cells were plated into each well of a 96-well clear flat-bottom, black polystyrene tissue-culture-treated plate at a density of ~10^4 cells per well, and plates were incubated overnight for adhesion. The day after plating, 1 μl of each compound, prepared as twofold serial dilutions of 5 mM stock solutions in DMSO, was added to each well. Cells were incubated for 3 days, after which resazurin was added to each well to a final concentration of 0.15 mM. After an additional 1 day of incubation, the fluorescence excitation/emission at 550/590 nm was read using a SpectraMax M3 plate reader. Experiments were performed in biological duplicate. IC_{50} values were determined by normalizing with respect to the fluorescence intensity values of untreated control cells on day 3, as described in 'Calculation of cellular viability values in dose–response curves' above.

Molecular docking simulations
Molecular docking simulations were performed using AutoDock Vina 1.2.0 (ref. 62), as we have done in previous work[79]. Compounds were provided as SMILES strings and represented in three dimensions using OpenBabel. Protein structures were curated from the PDB using the accession codes tabulated in Fig. 5a, and the coordinates of the bound inhibitors were retrieved using PyMOL to define the active site of each protein (as detailed further below). Next, AutoDockTools[83] (ver. 1.5.7) was used to prepare each protein and compound for docking, by converting each file into AutoDock Vina's PDBQT format. For compound preparation, hydrogen atoms were added at pH 7.4, and hydrated docking was used whenever possible. For protein preparation, the default prepare_receptor command was used. For each protein, the active site was based on the bounding box of the corresponding bound inhibitor from the PDB: the center of the active site was taken to coincide with the center of the bounding box, and the length of each edge of the bounding box was multiplied by a factor of 1.5 to specify the corresponding edge of the active site, to allow for broader conformational sampling. Docking was performed with a default exhaustiveness of 32, which specifies the number of runs that start with a random ligand conformation, and a default n_poses of 20, which specifies the final number of ligand poses to report. All binding affinities predicted by our docking simulations are reported in Fig. 5c. The predicted bound conformations shown in Fig. 5d were visualized using PyMOL (ver. 2.5.2).

BCL-2 TR-FRET
Inhibition of Bcl-2 binding to a peptide ligand was measured using the BCL-2 TR-FRET Assay Kit from BPS Bioscience (BPS Bioscience 50222). Briefly, the provided BCL TR-FRET assay buffer was diluted 1:3 with ultrapure Milli-Q water. The anti-His terbium-labeled donor and dye-labeled acceptor were each diluted 1:100 with diluted assay buffer. The BCL-2 peptide ligand was thawed on ice and diluted 1:40 with diluted assay buffer, and BCL-2 protein was diluted with diluted assay buffer to a working concentration of 1 ng μl^{-1}. Test compounds at the indicated final concentrations were prepared as stock 10% DMSO solutions in ultrapure Milli-Q water. The reaction was performed by combining 5 μl diluted donor, 5 μl diluted acceptor, 2 μl test compound, 5 μl diluted ligand and 3 μl diluted protein in each well of the provided white, flat-bottom 384-well plate. Positive control reactions had 2 μl 10% DMSO in water in lieu of test compound. Negative control reactions had 2 μl 10% DMSO in water and 5 μl diluted assay buffer in lieu of test compound and diluted ligand. Reactions were incubated at room temperature for 3 h, and fluorescence intensities were measured using a SpectraMax M5 plate reader and manufacturer software (SoftMax Pro 6) with the following TR-FRET settings: for terbium-labeled donor emission, excitation/emission, 340/620 nm; lag time, 100 μs; integration time, 500 μs; for dye-acceptor emission, excitation/emission, 340/665 nm; lag time, 100 μs; integration time, 500 μs. The TR-FRET ratio, 665 nm emission/620 nm emission, was calculated for all reactions, and percentage activity was calculated by linearly interpolating the positive and negative control TR-FRET ratio values between relative activity values of 0 and 1. Experiments were performed in biological duplicate and repeated on independent occasions.

Hemolysis assay
Following previous work[84], for the hemolysis experiments shown in Extended Data Fig. 8, whole human blood containing EDTA (Innovative Resarch IWB1K2E) was centrifuged at 120g at 4 °C for 5 min and resuspended in DPBS (VWR 02-0119-0500). These washing steps were repeated until the supernatant was clear. Red blood cells were then resuspended in DPBS to 5 × 10^8 cells ml^{-1}, and 100 μl of cells was plated into each well of a 96-well clear round-bottom plate. Compounds were added to the indicated concentrations, and DMSO was used as a vehicle. Samples were incubated for 1 h at 37 °C without shaking, after which plates were centrifuged at 1,500g at room temperature for 5 min to pellet cells. Sixty microliters of the supernatant from each sample was then transferred to a 96-well clear flat-bottom plate, and the absorbance was read at 405 nm using a SpectraMax M3 plate reader to quantify the amount of soluble hemoglobin. Fractional hemolysis was determined by linearly interpolating absorbance values with respect

to a positive control (saturation with 10% Triton X-100) and a negative control (1% DMSO vehicle).

Genotoxicity assay

For the mutagenesis experiments shown in Extended Data Fig. 8, an Ames 384-ISO test (6041-1S) from Environmental Bio-Detection Products was used following the manufacturer's instructions. Briefly, *Salmonella typhimurium* TA100 was grown overnight (16–18 h) at 37 °C with shaking at 300 r.p.m. and treated with the provided exposure media and compound samples at the final concentrations indicated. Treatment with the provided 4-nitroquinoline 1-oxide, a mutagen, was used as a positive control. Cells were then added to the provided reversion solution, and each sample was split into 48 wells of 384-well plates. Plates were incubated at 37 °C for 2 days, after which the number of revertant (yellow-colored) wells corresponding to each sample was counted. Additionally, we verified that each test compound did not inhibit the growth of *S. typhimurium* TA100. An overnight bacterial culture was diluted 1:10,000 in LB medium (Becton Dickinson 244620) and plated using 99 µl working volumes into the wells of a clear flat-bottom 96-well plate. One microliter of twofold dilutions of each test compound in DMSO, starting from a final concentration of 500 µM, was added across wells, and plates were sealed and incubated overnight at 37 °C to determine bacterial growth.

Aged mouse model experiments

For the baseline experiment shown in Fig. 6a–c, young (6–8-week-old) and aged (90-week-old) female C57BL/6J mice were procured from The Jackson Laboratory and quarantined at least 2 days before use. For the experiment shown in Fig. 6d–f, aged (80-week-old) female C57BL/6J mice were procured from The Jackson Laboratory and quarantined at least 2 days before use. Animals were housed in a facility maintained at 20–26 °C ambient temperature, 40–65% relative humidity and a 12:12 light–dark cycle. Enrichment devices were included in the animal environments as required and changed bi-weekly. All mice in this study were treated in accordance with protocol IS00000852-6, approved by Harvard Medical School Institutional Animal Care and Use Committee and the Committee on Microbiological Safety.

For compound administration, BRD-K56819078 (ChemBridge 7507010) was prepared fresh in 10% DMSO:45% PEG300:45% water for injection w/w, and for each mouse a total of six intraperitoneal injections over a 14 day period were performed at 25 mg kg^{-1} per injection, as determined by weighing each mouse immediately before injection. All mice were killed by CO_2 asphyxiation and dissected, and one kidney was collected per mouse. Each kidney was divided for SA-β-gal staining and mRNA measurements. Samples that were designated for SA-β-gal staining were embedded in optimal cutting temperature medium and flash-frozen in liquid nitrogen. Samples that were designated for mRNA measurements were placed in RNAlater Stabilization Solution (Thermo Fisher AM7021) and flash-frozen with dry ice.

For SA-β-gal staining, kidney samples were oriented and cut into 10-µm-thin sections using a Leica CM1950 cryostat. SA-β-gal staining was then performed similarly to the above, but with modifications. Frozen sections were fixed for 15 min using 2% formaldehyde and 0.2% glutaraldehyde in PBS (pH 7.4). Sections were then washed in PBS and incubated overnight at 37 °C in a dry incubator with β-gal staining solution, an aqueous solution containing 40 mM citric acid/sodium phosphate (MilliporeSigma C0759 and S9763), 5 mM potassium ferrocyanide (MilliporeSigma P9387), 5 mM potassium ferricyanide (MilliporeSigma P8131), 2 mM magnesium chloride (MilliporeSigma M8266), 150 mM sodium chloride (Fisher Scientific S271) and 1 mg ml^{-1} X-gal (MilliporeSigma 9660), titrated to pH 6.0, as described in previous work[4,85]. Sections were washed in PBS, counterstained with Nuclear Fast Red (VWR AAJ61010-AP) for 5 min at room temperature, then washed again in PBS before imaging. Imaging was performed on an EVOS XL Core or a Leica DMi1 equipped with a Flexacam C1 camera. Two fields

of view were captured for each kidney section, the images were thresholded by color using ImageJ ver. 2.0.0-rc-69/1.52p (National Institutes of Health) and the ratios of blue area (SA-β-gal-positive area) to total red and blue area (all cells) were calculated for each field of view. One kidney sample from each of the vehicle- and BRD-K56819078-treated aged mice groups failed to stain for SA-β-gal, which may arise if the sections did not contain any kidney cortical region[86]; data from these samples were discarded.

For mRNA measurements, kidney samples were homogenized using an SP Bel-Art ProCulture cordless homogenizer, and mRNA was extracted and quantified as described above in 'mRNA quantification using quantitative PCR', using a PureLink RNA Mini Kit (Thermo Fisher 12183020) for extraction. The following primers were used, and the relative expression of each gene was determined by normalization to β-actin expression for each sample:

p16 forward primer: AGGGCCGTGTGCATGACGTG
p16 reverse primer: GCACCGGGCGGGAGAAGGTA
p21 forward primer: AACATCTCAGGGCCGAAA
p21 reverse primer: TGCGCTTGGAGTGATAGAAA
β-Actin forward primer: GGCTGTATTCCCCTCCATCG
β-Actin reverse primer: CCAGTTGGTAACAATGCCATGT

Statistics and reproducibility

No statistical method was used to predetermine sample size for all experiments in this study, but our sample sizes are similar to those reported in previous publications (refs. 3–8). We were not blinded to allocation during experiments and outcome assessment, and data collection and analysis were not performed blind to the conditions of the experiments. For mouse experiments, no substantial bias was observed across initial groups. No data were excluded from the analyses in this study, with the exception of one kidney sample from each of the vehicle- and BRD-K56819078-treated aged mice groups for SA-β-gal experiments (as detailed above in 'Aged mouse model experiments').

Two-sided, two-sample unpaired *t*-tests or one-way analysis of variance tests were performed using MATLAB in Figs. 1c and 4b and Extended Data Fig. 7 to test the hypothesis that mRNA expression values for p16, p21 and KI67 were different from control (vehicle-treated or early passage) cell values in the therapy-induced and replicative senescence models. Two-sided, two-sample unpaired *t*-tests were performed using MATLAB in Fig. 5e to test the hypothesis that the Bcl-2 activity values in each treatment condition have mean values different from that of corresponding positive control measurements (relative Bcl-2 activity values of 1). One-sided, two-sample permutation tests for differences in mean value[87] were performed using MATLAB in Fig. 6c,e,f to test the hypothesis that SA-β-gal-positive areas or mRNA expression values for p16 and p21 were different from control (naïve aged mice or vehicle-treated aged mice) values for mouse model experiments. Exact permutation tests, in which all possible combinations were considered, were used for all comparisons with the exception of Fig. 6e, for which 100,000 random combinations were used due to the larger sample sizes. Where relevant, data distribution was assumed to be normal, but this was not formally tested.

Reporting summary

Further information on research design is available in the Nature Portfolio Reporting Summary linked to this article.

Data availability

Data generated from chemical screens, machine learning models and computational analyses are available as Supplementary Data 1–4. For molecular docking studies, protein structures from accession codes 6qgh (Bcl-2), 3wiz (Bcl-XL), 1osf (Hsp90), 4hg7 (MDM2) and 4f1s (PI3K) were obtained from the PDB at https://www.rcsb.org/. All other data are available from the corresponding author upon request. Source Data are provided with this paper.

Code availability

Chemprop is publicly available at https://github.com/chemprop/chemprop. A detailed code platform, including a Jupyter notebook and the Chemprop checkpoints for the different models developed in this work, is publicly available at https://github.com/felixjwong/senolyticsai.

References

1. Niedernhofer, L. J. & Robbins, P. D. Senotherapeutics for healthy aging. *Nat. Rev. Drug Disc.* **17**, 377 (2018).
2. Childs, B. G. et al. Senescent cells: an emerging target for diseases of ageing. *Nat. Rev. Drug Disc.* **16**, 718–735 (2017).
3. Baker, D. J. et al. Clearance of p16^Ink4a-positive senescent cells delays ageing-associated disorders. *Nature* **479**, 232–236 (2011).
4. Johmura, Y. et al. Senolysis by glutaminolysis inhibition ameliorates various age-associated disorders. *Science* **371**, 265–270 (2021).
5. Xu, M. et al. Senolytics improve physical function and increase lifespan in old age. *Nat. Med.* **24**, 1246–1256 (2018).
6. Fuhrmann-Stroissnigg, H. et al. Identification of HSP90 inhibitors as a novel class of senolytics. *Nat. Commun.* **8**, 422 (2017).
7. Guerrero, A. et al. Cardiac glycosides are broad-spectrum senolytics. *Nat. Metab.* **1**, 1074–1088 (2019).
8. Wakita, M. et al. A BET family protein degrader provokes senolysis by targeting NHEJ and autophagy in senescent cells. *Nat. Commun.* **11**, 1935 (2020).
9. Xu, Q. et al. The flavonoid procyanidin C1 has senotherapeutic activity and increases lifespan in mice. *Nat. Metab.* **3**, 1706–1726 (2021).
10. Robbins, P. D. Senolytic drugs: reducing senescent cell viability to extend health span. *Annu. Rev. Pharmacol. Toxicol.* **61**, 779–803 (2021).
11. Demaria, M. et al. An essential role for senescent cells in optimal wound healing through secretion of PDGF-AA. *Dev. Cell* **31**, 722–733 (2014).
12. Grosse, L. et al. Defined p16^High senescent cell types are indispensable for mouse healthspan. *Cell Metab.* **32**, 87–99 (2020).
13. Zhu, Y. et al. The Achilles' heel of senescent cells: from transcriptome to senolytic drugs. *Aging Cell* **14**, 644–658 (2015).
14. Zhu, Y. et al. Identification of a novel senolytic agent, navitoclax, targeting the Bcl-2 family of anti-apoptotic factors. *Aging Cell* **15**, 428–435 (2016).
15. Yosef, R. et al. Directed elimination of senescent cells by inhibition of BCL-W and BCL-XL. *Nat. Commun.* **7**, 11190 (2016).
16. Kirkland, J. K. & Tchkonia, T. Senolytic drugs: from discovery to translation. *J. Intern. Med.* **288**, 518–536 (2020).
17. Triana-Martínez, F. et al. Identification and characterization of cardiac glycosides as senolytic compounds. *Nat. Commun.* **10**, 4731 (2019).
18. Rudin, C. M. et al. Phase II study of single-agent navitoclax (ABT-263) and biomarker correlates in patients with relapsed small cell lung cancer. *Clin. Cancer Res.* **18**, 3163–3169 (2012).
19. Vamathevan, J. et al. Applications of machine learning in drug discovery and development. *Nat. Rev. Drug Disc.* **18**, 463–477 (2019).
20. Mamoshina, P., Vieira, A., Putin, E. & Zhavoronkov, A. Applications of deep learning in biomedicine. *Mol. Pharm.* **13**, 1445–1454 (2016).
21. Zhavoronkov, A. et al. Artificial intelligence for aging and longevity research: recent advances and perspectives. *Ageing Res. Rev.* **49**, 49–66 (2019).
22. Moskalev, A., Chernyagina, E., Kudryavtseva, A. & Shaposhnikov, M. Geroprotectors: a unified concept and screening approaches. *Aging Dis.* **8**, 354–363 (2017).
23. Stokes, J. M. et al. A deep learning approach to antibiotic discovery. *Cell* **180**, 688–702 (2020).
24. Ma, Y. et al. Identification of antimicrobial peptides from the human gut microbiome using deep learning. *Nat. Biotech.* **40**, 921–931 (2022).
25. Aliper, A. et al. Deep learning applications for predicting pharmacological properties of drugs and drug repurposing using transcriptomic data. *Mol. Pharm.* **13**, 2524–2530 (2016).
26. Mayr, A. et al. Large-scale comparison of machine learning methods for drug target prediction on ChEMBL. *Chem. Sci.* **24**, 5441–5451 (2018).
27. Bagherian, M. et al. Machine learning approaches and databases for prediction of drug–target interaction: a survey paper. *Brief Bioinform.* **22**, 247–269 (2021).
28. Putin, E. et al. Deep biomarkers of human aging: application of deep neural networks to biomarker development. *Aging* **8**, 1021–1030 (2016).
29. Zhavoronkov, A., Li, R., Ma, C. & Mamoshina, P. Deep biomarkers of aging and longevity: from research to applications. *Aging* **11**, 10771–10780 (2019).
30. Mamoshina, P. et al. Machine learning on human muscle transcriptomic data for biomarker discovery and tissue-specific drug target identification. *Front. Genet.* **9**, 242 (2018).
31. Zhavoronkov, A. et al. Deep learning enables rapid identification of potent DDR1 kinase inhibitors. *Nat. Biotech.* **37**, 1038–1040 (2019).
32. Popa, M., Isayev, O. & Tropsha, A. Deep reinforcement learning for de novo drug design. *Sci. Adv.* **4**, eaap7885 (2018).
33. Olivecrona, M., Blaschke, T., Engkvist, O. & Chen, H. Molecular de-novo design through deep reinforcement learning. *J. Cheminform.* **9**, 48 (2017).
34. Yang, K. et al. Analyzing learned molecular representations for property prediction. *J. Chem. Inf. Model.* **59**, 3370–3388 (2019).
35. Lal, A. et al. p16^INK4a translation suppressed by miR-24. *PLoS ONE* **3**, e1864 (2008).
36. Omori, S. et al. Generation of a p16 reporter mouse and its use to characterize and target p16^high cells in vivo. *Cell Metab.* **3**, 814–828 (2020).
37. Liu, J.-Y. et al. Cells exhibiting strong p16^INK4a promoter activation in vivo display features of senescence. *Proc. Natl Acad. Sci. USA* **116**, 2603–2611 (2019).
38. Kirschner, K. et al. Phenotype specific analyses reveal distinct regulatory mechanism for chronically activated p53. *PLoS Genet.* **19**, e1005053 (2015).
39. Gerdes, J. et al. Cell cycle analysis of a cell proliferation-associated human nuclear antigen defined by the monoclonal antibody Ki-67. *J. Immunol.* **133**, 1710–1715 (1984).
40. Uxa, S. et al. Ki-67 gene expression. *Cell Death Diff.* **28**, 3357–3370 (2021).
41. Corsello, S. M. et al. The Drug Repurposing Hub: a next-generation drug library and information resource. *Nat. Med.* **23**, 405–408 (2017).
42. Van der Maaten, L. & Hinton, G. Visualizing data using t-SNE. *J. Mach. Learn. Res.* **9**, 2579–2605 (2008).
43. Baell, J. B. & Holloway, G. A. New substructure filters for removal of pan assay interference compounds (PAINS) from screening libraries and for their exclusion in bioassays. *J. Med. Chem.* **53**, 2719–2740 (2010).
44. Brenk, R. et al. Lessons learnt from assembling screening libraries for drug discovery for neglected diseases. *ChemMedChem* **3**, 435–444 (2008).
45. Lipinski, C. A., Lombardo, F., Dominy, B. W. & Feeney, P. J. Experimental and computational approaches to estimate solubility and permeability in drug discovery and development settings. *Adv. Drug Disc. Rev.* **23**, 3–25 (1997).

46. Karpinich, N. O., Tafani, M., Rothman, R. J., Russo, M. A. & Farber, J. L. The course of etoposide-induced apoptosis from damage to DNA and p53 activation to mitochondrial release of cytochrome c. *J. Biol. Chem.* **277**, 16547–16552 (2002).

47. Jamil, S., Lam, I., Majd, M., Tsai, S.-H. & Duronio, V. Etoposide induces cell death via mitochondrial-dependent actions of p53. *Cancer Cell Int.* **15**, 79 (2015).

48. Veber, D. F. et al. Molecular properties that influence the oral bioavailability of drug candidates. *J. Med. Chem.* **45**, 2615–2623 (2002).

49. Wu, Y. et al. Senolytics: eliminating senescent cells and alleviating intervertebral disc degeneration. *Front. Bioeng. Biotechnol.* **10**, 823945 (2022).

50. Wang, L. et al. Discovery of A-1331852, a first-in-class, potent, and orally-bioavailable BCL-X$_L$ inhibitor. *ACS Med. Chem. Lett.* **11**, 1829–1836 (2020).

51. Youle, R. J. & Strasser, A. The BCL-2 protein family: opposing activities that mediate cell death. *Nat. Rev. Mol. Cell Biol.* **9**, 47–59 (2008).

52. Schopf, F. H., Biebl, M. M. & Buchner, J. The HSP90 chaperone machinery. *Nat. Rev. Mol. Cell Biol.* **18**, 345–360 (2017).

53. Fuhrmann-Stroissnigg, H., Niedernhofer, L. J. & Robbins, P. D. Hsp90 inhibitors as senolytic drugs to extend healthy aging. *Cell Cycle* **17**, 1048–1055 (2018).

54. Shangary, S. & Wang, S. Targeting the MDM2–p53 interaction for cancer therapy. *Clin. Cancer Res.* **14**, 5318–5324 (2008).

55. Chène, P. Inhibiting the p53–MDM2 interaction: an important target for cancer therapy. *Nat. Rev. Cancer* **3**, 102–109 (2003).

56. Wang, L., Lankhorst, L. & Bernards, R. Exploiting senescence for the treatment of cancer. *Nat. Rev. Cancer* **22**, 340–355 (2022).

57. Pawge, G. & Khatik, G. L. p53 regulated senescence mechanism and role of its modulators in age-related disorders. *Biochem. Pharmacol.* **190**, 114651 (2021).

58. Porta, C., Paglino, C. & Mosca, A. Targeting PI3K/Akt/mTOR signaling in cancer. *Front. Oncol.* **4**, 64 (2014).

59. Kirkland, J. L., Tchkonia, T., Zhu, Y., Niedernhofer, L. J. & Robbins, P. D. The clinical potential of senolytic drugs. *J. Am. Geriatr. Soc.* **65**, 2297–2301 (2017).

60. Lozano-Torres, B. et al. The chemistry of senescence. *Nat. Rev. Chem.* **3**, 426–441 (2019).

61. Lim, J. Y., Lee, J. Y., Byun, B. J. & Kim, S. W. Fisetin targets phosphatidylinositol-3-kinase and induces apoptosis of human B lymphoma Raji cells. *Toxicol. Rep.* **2**, 984–989 (2015).

62. Eberhardt, J., Santos-Martins, D., Tillack, A. F. & Forli, S. AutoDock Vina 1.2.0: new docking methods, expanded force field, and Python bindings. *J. Chem. Inf. Model.* **61**, 3891–3898 (2021).

63. Murray, J. B. et al. Establishing drug discovery and identification of hit series for the anti-apoptotic proteins, Bcl-2 and Mcl-1. *ACS Omega* **4**, 8892–8906 (2019).

64. Tanaka, Y. et al. Discovery of potent Mcl-1/Bcl-xL dual inhibitors by using a hybridization strategy based on structural analysis of target proteins. *J. Med. Chem.* **56**, 9635–9645 (2013).

65. Jez, J. M., Chen, J. C., Rastelli, G., Stroud, R. M. & Santi, D. V. Crystal structure and molecular modeling of 17-DMAG in complex with human Hsp90. *Chem. Biol.* **10**, 361–368 (2003).

66. Anil, B., Riedinger, C., Endicott, J. A. & Noble, M. E. The structure of an MDM2-nutlin-3a complex solved by the use of a validated MDM2 surface-entropy reduction mutant. *Acta Crystallogr. D* **69**, 1358–1366 (2013).

67. Wurz, R. P. et al. Synthesis and structure–activity relationships of dual PI3K/mTOR inhibitors based on a 4-amino-6-methyl-1,3,5-triazine sulfonamide scaffold. *Bioorg. Med. Chem. Lett.* **22**, 5714–5720 (2012).

68. Ha, J.-Y. Molecular mimicry-based repositioning of nutlin-3 to anti-apoptotic Bcl-2 family proteins. *J. Am. Chem. Soc.* **133**, 1244–1247 (2011).

69. Novais, E. J. et al. Long-term treatment with senolytic drugs dasatinib and quercetin ameliorates age-dependent intervertebral disc degeneration in mice. *Nat. Commun.* **12**, 5213 (2021).

70. He, Y. et al. Using proteolysis-targeting chimera technology to reduce navitoclax platelet toxicity and improve its senolytic activity. *Nat. Commun.* **11**, 1996 (2020).

71. Chang, J. et al. Clearance of senescent cells by ABT263 rejuvenates aged hematopoietic stem cells in mice. *Nat. Med.* **22**, 78–83 (2016).

72. Mylonas, K. J. et al. Cellular senescence inhibits renal regeneration after injury in mice, with senolytic treatment promoting repair. *Sci. Trans. Med.* **13**, abb0203 (2021).

73. Idda, M. L. et al. Survey of senescent cell markers with age in human tissues. *Aging* **12**, 4052–4066 (2020).

74. Öztürk, H., Özgür, A. & Ozkirimli, E. DeepDTA: deep drug–target binding affinity prediction. *Bioinformatics* **34**, i821–i829 (2018).

75. Thafar, M. A. et al. Affinity2Vec: drug–target binding affinity prediction through representation learning, graph mining, and machine learning. *Sci Rep.* **12**, 4751 (2022).

76. He, T., Heidemeyer, M., Ban, F., Cherkasov, A. & Ester, M. SimBoost: a read-across approach for predicting drug–target binding affinities using gradient boosting machines. *J. Cheminform.* **9**, 24 (2017).

77. Adeshina, Y. O., Deeds, E. J. & Karanicolas, J. Machine learning classification can reduce false positives in structure-based virtual screening. *Proc. Natl Acad. Sci. USA* **117**, 18477–18488 (2020).

78. Bender, B. J. et al. A practical guide to large-scale docking. *Nat. Protoc.* **16**, 4799–4832 (2021).

79. Wong, F. et al. Benchmarking AlphaFold-enabled molecular docking predictions for antibiotic discovery. *Mol. Syst. Biol.* **18**, e11081 (2022).

80. Jiménez-Luna, J., Grisoni, F. & Schneider, G. Drug discovery with explainable artificial intelligence. *Nat. Mach. Intell.* **2**, 573–584 (2020).

81. Karin, O., Agrawal, A., Porat, Z., Krizhanovsky, V. & Alon, U. Senescent cell turnover slows with age providing an explanation for the Gompertz law. *Nat. Commun.* **10**, 5495 (2019).

82. Daina, A., Michielin, O. & Zoete, V. SwissADME: a free web tool to evaluate pharmacokinetics, drug-likeness and medicinal chemistry friendliness of small molecules. *Sci. Rep.* **7**, 42717 (2017).

83. Morris, G. M. et al. AutoDock4 and AutoDockTools4: automated docking with selective receptor flexibility. *J. Comput. Chem.* **30**, 2785–2791 (2009).

84. Greco, I. et al. Correlation between hemolytic activity, cytotoxicity and systemic in vivo toxicity of synthetic antimicrobial peptides. *Sci. Rep.* **6**, 13206 (2020).

85. Dimri, G. P. et al. A biomarker that identifies senescent human cells in culture and in aging skin in vivo. *Proc. Natl Acad. Sci. USA* **92**, 9363–9367 (1995).

86. Valentijn, F. A., Falke, L. L., Nguyen, T. Q. & Goldschmeding, R. Cellular senescence in the aging and diseased kidney. *J. Cell Commun. Signal.* **12**, 69–82 (2018).

87. Krol, L. R. Permutation test. *GitHub* https://github.com/lrkrol/permutationTest (2022).

Acknowledgements

Author contributions

F.W. conceived research, designed models and experiments, performed experiments and analysis, wrote the paper and supervised research. S.O. and N.M.D. designed and performed experiments and analysis. E.J.Z. assisted with experiments. J.J.C. supervised research. All authors assisted with manuscript editing.

Competing interests

J.J.C. is an academic co-founder and board member of Cellarity, and the founding Scientific Advisory Board chair of Integrated Biosciences. F.W. is a co-founder of Integrated Biosciences. The remaining authors declare no competing interests.

Additional information

Extended data is available for this paper at https://doi.org/10.1038/s43587-023-00415-z.

Supplementary information The online version contains supplementary material available at https://doi.org/10.1038/s43587-023-00415-z.

Day -6   Day -4   Day 0   Day 1   Day 4   Day 5

Vehicle/etoposide treatment for 2 days

Media replaced for cell recovery

Cells seeded

Compounds added

Resazurin reduction assay

Read fluorescence (cell viability)

Extended Data Fig. 1 | Timeline of etoposide-induced senescence. Control (DMSO-treated) and senescent (etoposide-treated) cells were treated with test compounds and assayed for cellular viability at the indicated times for compound screening and dose-response experiments.
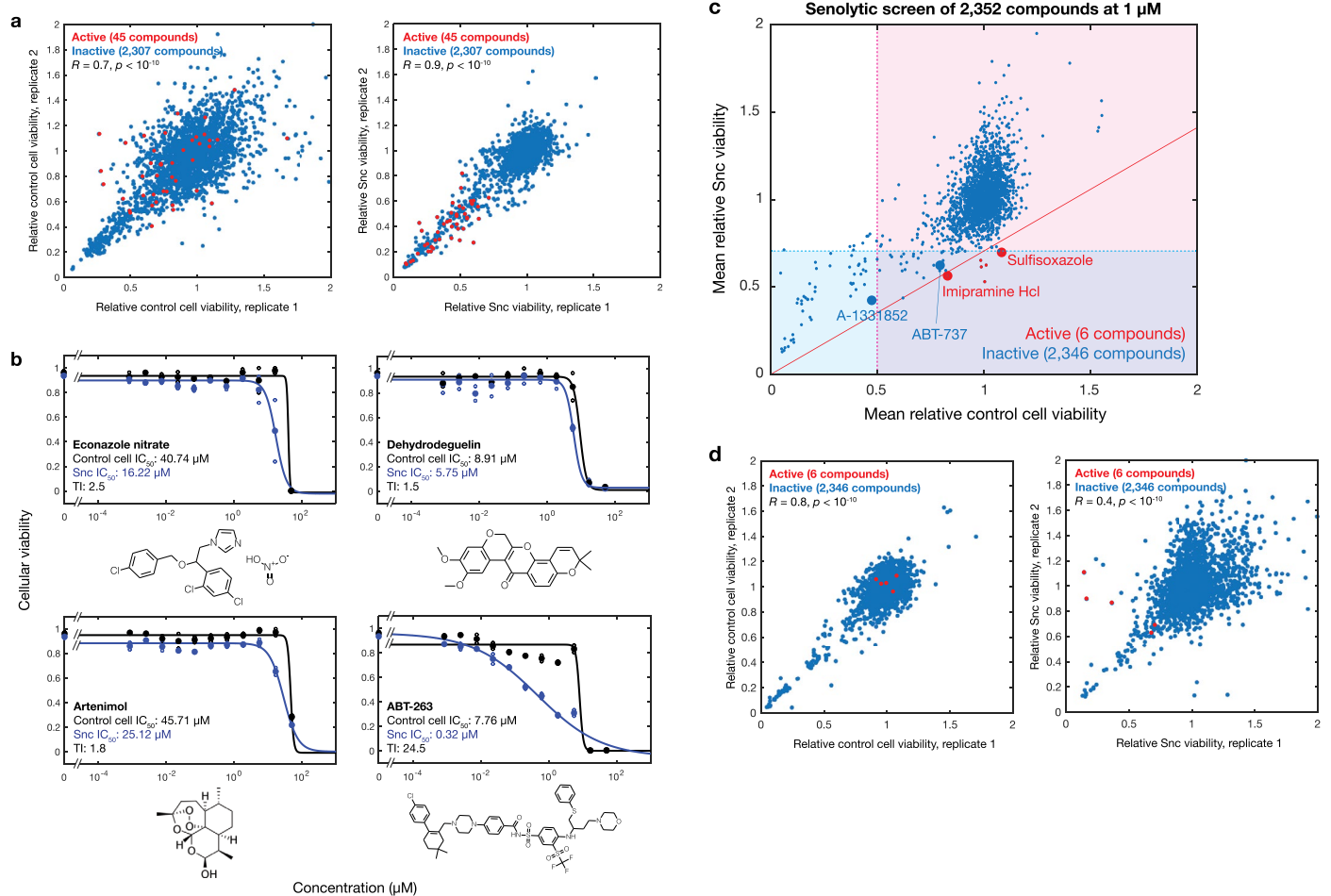
Extended Data Fig. 2 | Screening of 2,352 compounds for senolytic activity and validation of four active compounds. a, Cellular viability of vehicle- and etoposide-treated cells after a 3-day course of test compound treatment (10 μM). Values are from two biological replicates, and viability measurements are normalized by the interquartile mean of each cell plate. Active compounds (red points) are those for which the relative control cell viability is >0.5, the relative Snc viability is <0.7, and the ratio of Snc to control cell viability is <0.7. All other compounds are inactive (blue points). The Pearson's correlation coefficient, R, and two-sided p-value are shown. **b**, Dose-response curves of control and etoposide-treated IMR-90 cells, treated with each compound shown. Zero μM (1% DMSO vehicle) treatment was included. Values are normalized by the average of two untreated samples from the same phenotype: here, a cellular viability of 1 indicates that of either untreated control cells or Sncs. Black curves indicate control (vehicle-treated) cells, and blue curves indicate (etoposide-treated) Sncs. Measurements are shown for two biological replicates in each treatment group (open points), and mean viability values (closed points) were fitted to calculate IC_{50} values. The therapeutic index (TI) is the ratio of IC_{50} values for vehicle- and etoposide-treated cells. The chemical structure of each compound is shown at the bottom of each plot. Note that, with our criteria for activity, ABT-263 has borderline activity at 1 μM and was inactive in our screen at 1 μM (panel (**c**)), due to marginal decreases in Snc viability. **c**, Senolytic screening results for 2,352 compounds at a final concentration of 1 μM. Values indicate the mean of two biological replicates, and viability measurements are normalized by the interquartile mean of each cell plate. Active and inactive compounds (red and blue points, respectively) are designated as in (**a**). Two known senolytics, ABT-737 and A-1331852, are inactive and highlighted with large blue points, and two active compounds, sulfisoxazole and imipramine hydrochloride, are highlighted with large red points. Sncs were induced with etoposide, and control cells were treated with vehicle (0.5% DMSO). **d**, Similar to (**a**), but for the screen shown in (**c**).
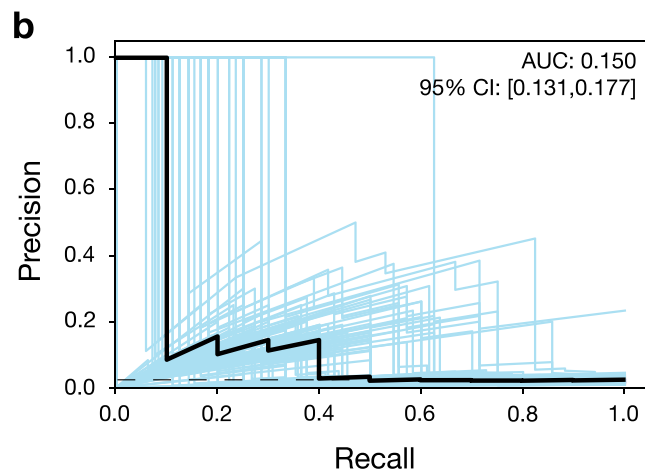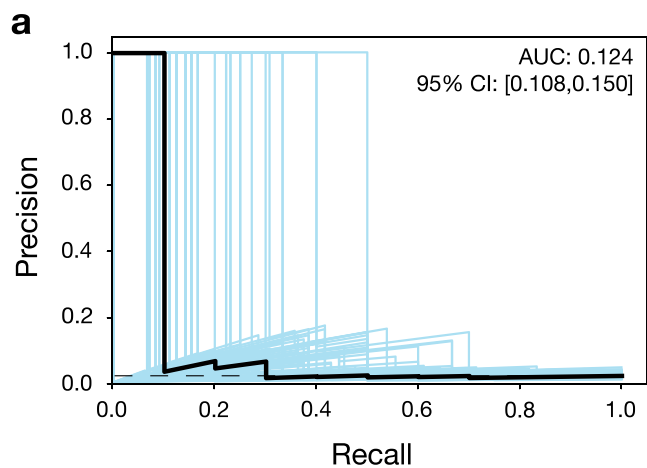
Extended Data Fig. 3 | Comparison of machine learning models. Shown are precision-recall curves for the two-best random forest models, trained and tested on the data shown in Fig. 1d. The black dashed curves represent the baseline fraction of active compounds in the training set (1.9%). Blue curves and the 95% confidence interval (CI) indicate the variation generated by bootstrapping. AUC, area under the precision-recall curve. The model hyperparameters used were: **a**, max depth, 5; number of estimators, 80; max features, 20; **b**, max depth, 5; number of estimators, 40; max features, 40.

Drug Repurposing Hub

Total compounds: 5,819
Activity score >0.4: 28
PAINS and Brenk filters: 18
Tanimoto filter: 10

Extended Broad Institute library

Total compounds: 799,140
Activity score >0.4: 2,537
PAINS and Brenk filters: 1,875
Tanimoto filter: 1,857

10 predicted active compounds from Drug Repurposing Hub
206 predicted active compounds from Extended Broad Institute library
50 predicted inactive compounds from Drug Repurposing Hub

Extended Data Fig. 4 | Chemical filters for favorable medicinal chemistry properties and structural novelty. The numbers of compounds after each chemical filtering step are shown, for both the Broad Institute Drug Repurposing Hub and the extended Broad Institute library. Numbers of curated compounds are indicated at bottom.
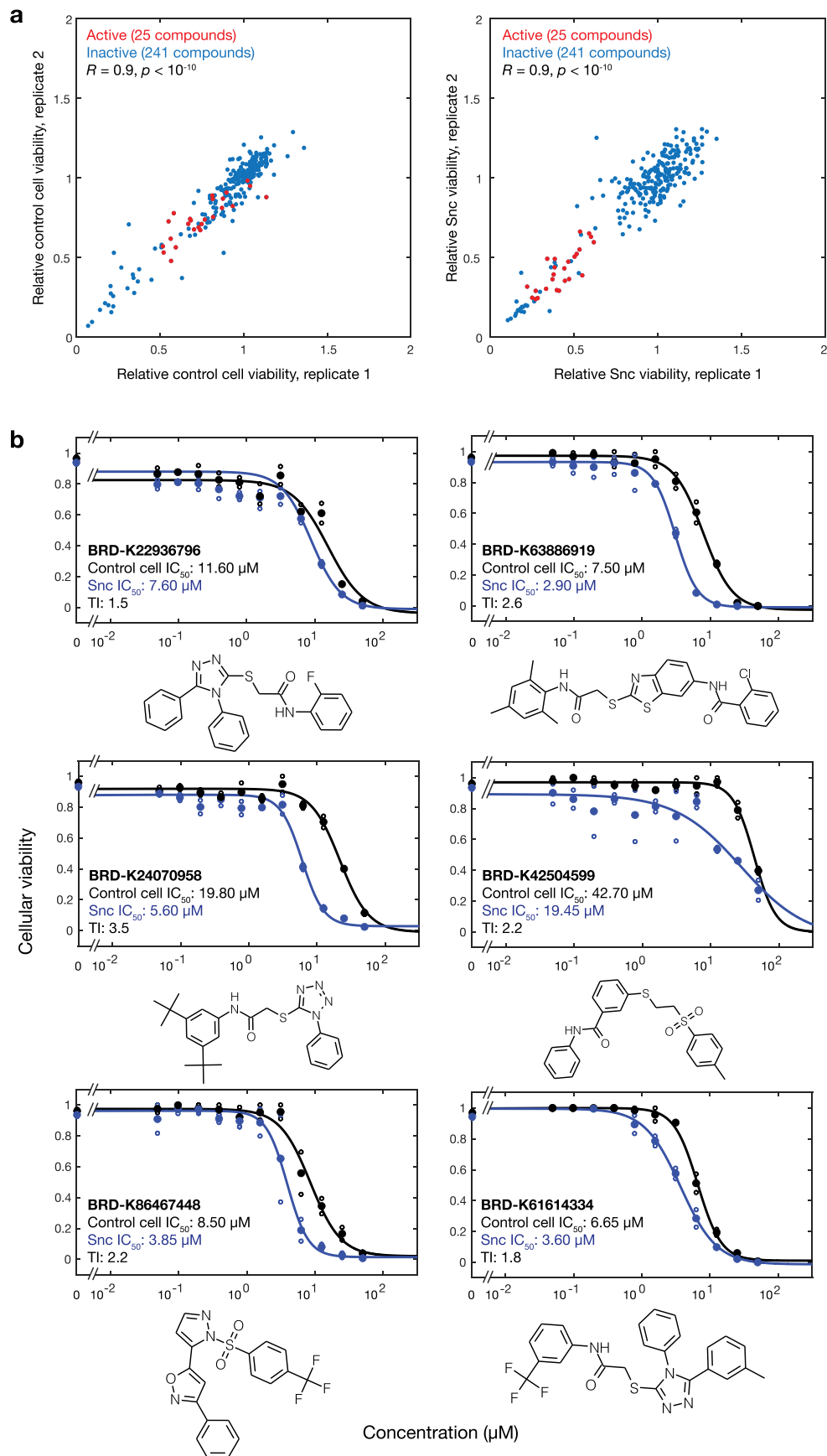
Extended Data Fig. 5 | See next page for caption.

Extended Data Fig. 5 | Screening of 216 compounds with high predicted senolytic activity, 50 compounds with low predicted senolytic activity, and validation of six additional active compounds. a, Relative viability of vehicle- and etoposide-treated cells after a 3-day course of test compound treatment (10 µM). Values are from two biological replicates, and viability measurements are normalized by the interquartile mean of each cell plate. Active compounds (red points) are those for which relative control cell viability is >0.5, relative Snc viability is <0.7, and the ratio of Snc to control cell viability is <0.7. All other compounds are inactive (blue points). The Pearson's correlation coefficient, R, and two-sided p-value are shown. **b**, Dose-response curves of control and etoposide-treated IMR-90 cells, treated with each compound shown. Compounds were serially diluted twofold starting from a final concentration of 50 µM, and 0 µM (1% DMSO vehicle) treatment was included. Cells were treated for 3 days. Cellular viability was determined by the metabolic reduction of resazurin into fluorescent resorufin, and values are normalized by the fluorescence intensities of the average of two untreated samples from the same phenotype: here, a cellular viability of 1 indicates that of either untreated control cells or Sncs. Vehicle treatment may result in cellular viability values <1 due to minor effects of DMSO on cellular viability. Black curves indicate control (vehicle-treated) cells, and blue curves indicate (etoposide-treated) Sncs. Measurements are shown for two biological replicates in each treatment group (open points), and mean viability values (closed points) were fitted to calculate IC_{50} values. The therapeutic index (TI) is the ratio of IC_{50} values for vehicle- and etoposide-treated cells. The chemical structure of each compound is shown at the bottom of each plot.
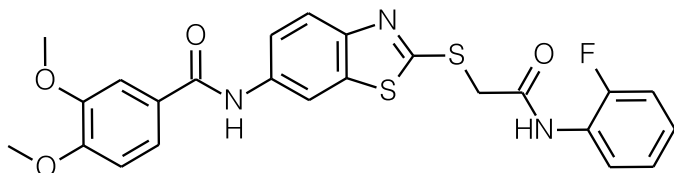
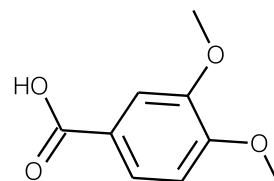# BRD-K20733377
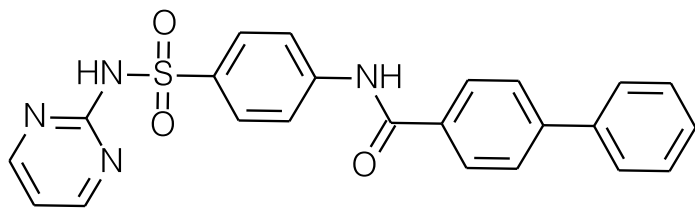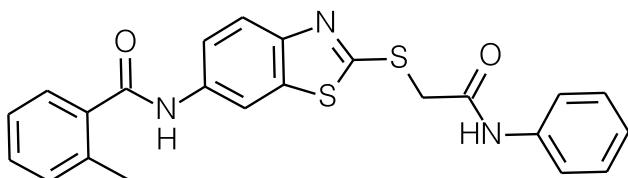
Sulfadiazine

Tanimoto similarity: 0.49
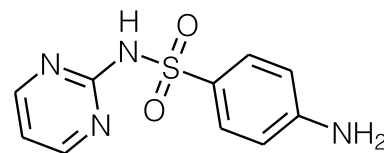
BRD-K56819078

3,4-dimethoxybenzoic acid

Tanimoto similarity: 0.29

BRD-K44839765

Salicylanilide
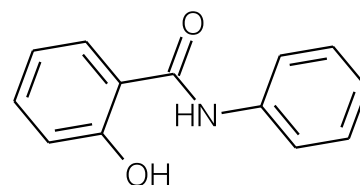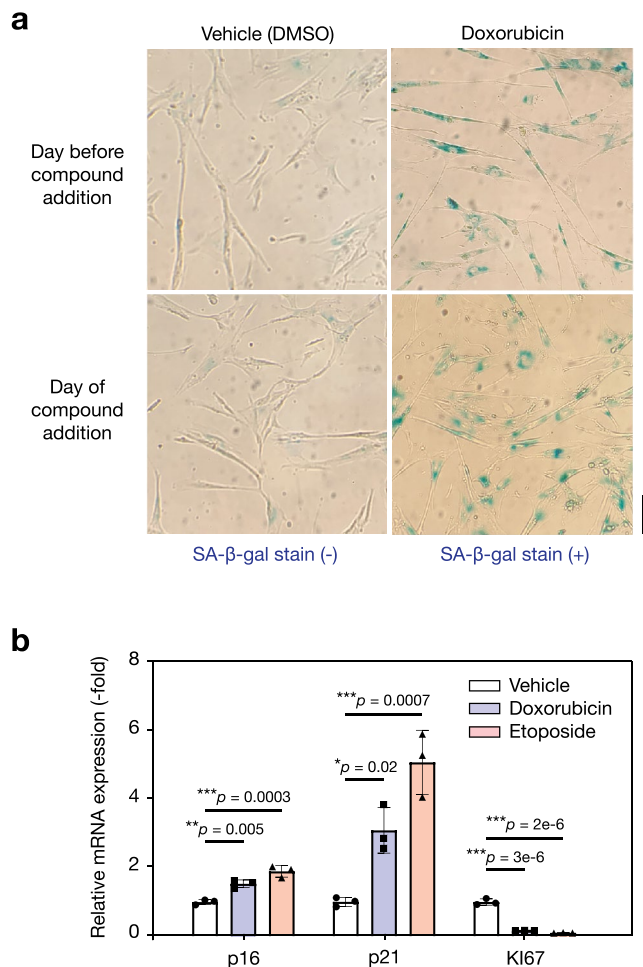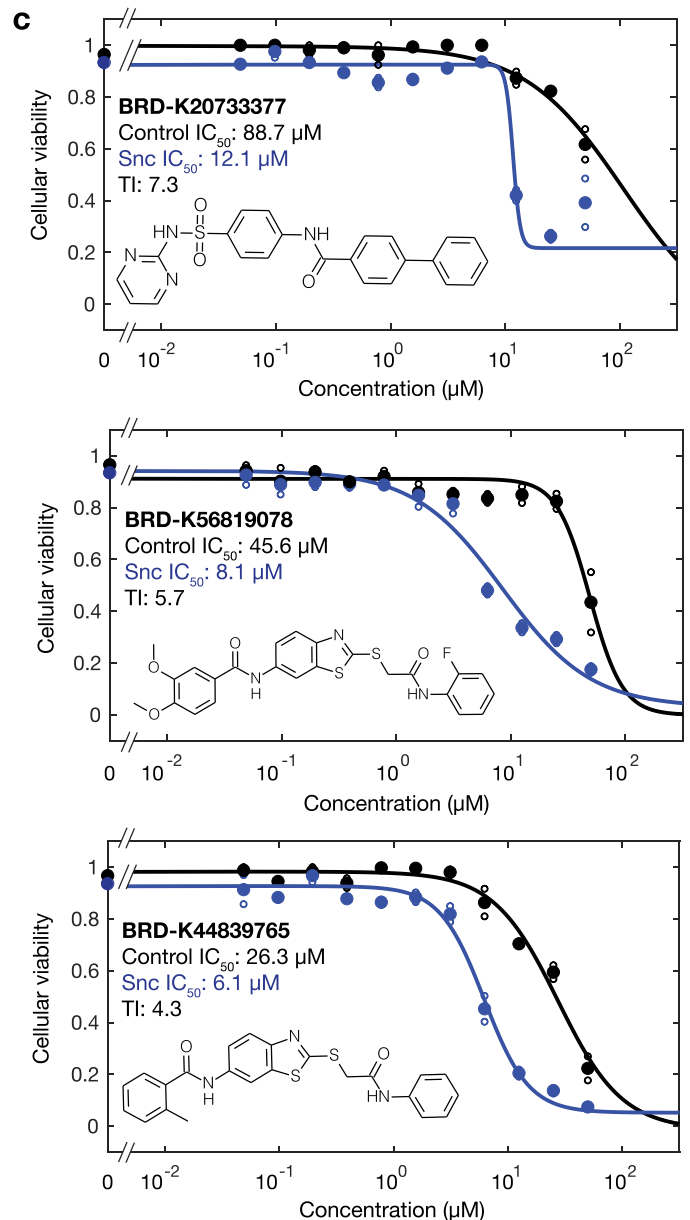
Tanimoto similarity: 0.34

Extended Data Fig. 6 | Structural comparisons of identified compounds. Shown are the compounds in the training dataset with highest structural similarity to each of BRD-K20733377, BRD-K56819078, and BRD-K44839765, as measured by the Tanimoto similarity.
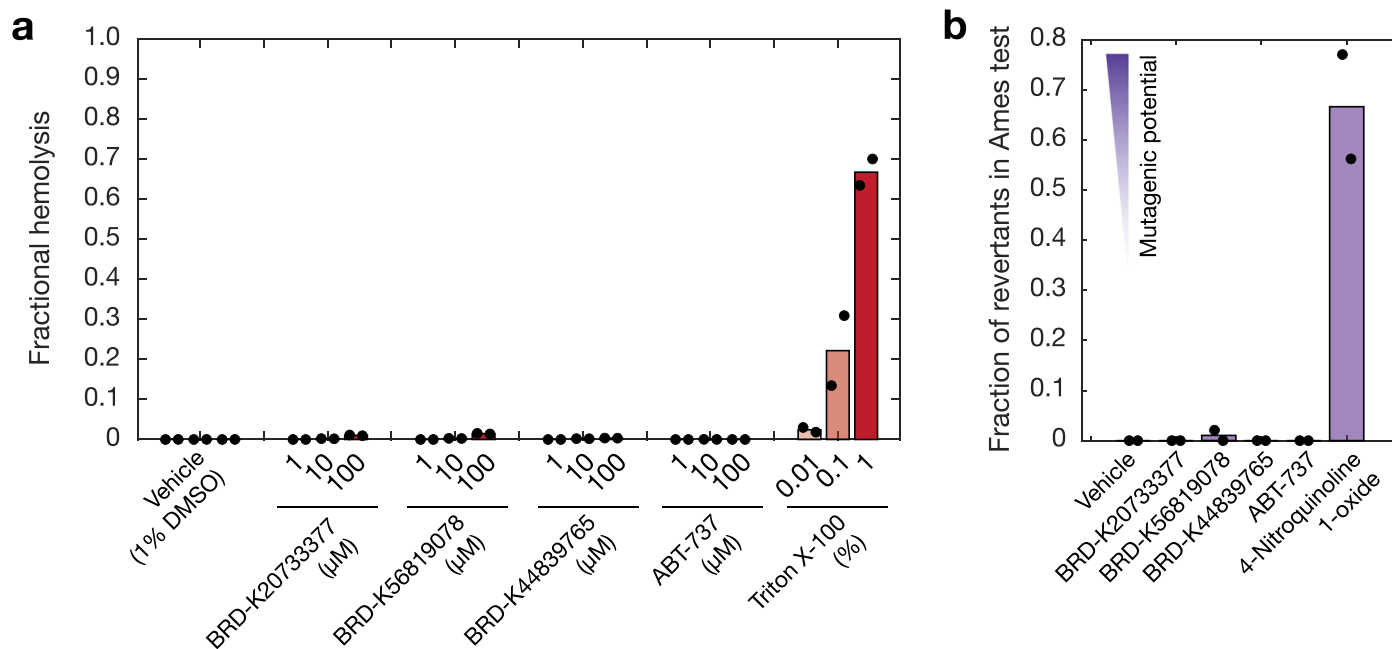
Extended Data Fig. 7 | BRD-K20733377, BRD-K56819078, and BRD-K44839765 exhibit senolytic activity in a model of doxorubicin-induced senescence.
a, SA-β-gal staining of vehicle- (0.5% DMSO) and doxorubicin-treated IMR-90 cells plated at times on corresponding to the day before and day of compound addition (see also Fig. 1b and Extended Data Fig. 1). Each image is representative of two biological replicates. Scale bar, 100 μm. **b**, Relative mRNA expression of p16, p21, and KI67 in vehicle- (0.5% DMSO), doxorubicin-, and etoposide-treated IMR-90 cells harvested on the day of compound addition. Data for vehicle-and etoposide-treated cells are identical to those shown in Fig. 1c of the main text, and are shown here for comparison. Data from three biological replicates are shown. Error bars indicate one standard deviation. One-way, two-sided ANOVA with Tukey's multiple comparisons: *$p \leq 0.05$, **$p < 0.01$, ***$p < 0.001$. **c**, Dose-response curves of control and doxorubicin-treated IMR-90 cells, treated with each compound shown. Compounds were serially diluted twofold starting from a final

concentration of 50 μM, and 0 μM (1% DMSO vehicle) treatment was included. Cells were treated for 3 days. Cellular viability was determined by the metabolic reduction of resazurin into fluorescent resorufin, and values are normalized by the fluorescence intensities of the average of two untreated samples from the same phenotype: here, a cellular viability of 1 indicates that of either untreated control cells or Sncs. Vehicle treatment may result in cellular viability values <1 due to minor effects of DMSO on cellular viability. Black curves indicate control (vehicle-treated) cells, and blue curves indicate (doxorubicin-treated) Sncs. Measurements are shown for two biological replicates in each treatment group (open points), and mean viability values (closed points) were fitted to calculate IC_{50} values. The therapeutic index (TI) is the ratio of IC_{50} values for vehicle- and doxorubicin-treated cells. The chemical structure of each compound is displayed in each inset. Data for control cells are identical to those shown in Fig. 3a–d of the main text.

Extended Data Fig. 8 | Preliminary assessments of compound toxicological properties. a, Fractional hemolysis measurements of human red blood cells treated with BRD-K20733377, BRD-K56819078, BRD-K44839765, and ABT-737 at the indicated final concentrations. Vehicle (1% DMSO) was used as a negative control, and Triton X-100 was used as a positive control. Black points indicate values from individual biological replicates, and red bars indicate average values. **b**, Ames test mutagenesis measurements of the fractions of revertant

S. typhimurium TA100 cultures treated with BRD-K20733377, BRD-K56819078, BRD-K44839765, and ABT-737 at a final concentration of 100 μM. Vehicle (1% DMSO) was used as a negative control, and 0.25 μg/mL (~1 μM) 4-nitroquinoline 1-oxide was used as a positive control. Black points indicate values from individual biological replicates, and purple bars indicate average values. Higher fractions of revertant cultures indicate higher mutagenic potential.

nature portfolio

Corresponding author(s):   James J. Collins

Last updated by author(s):   Feb 21, 2023

Reporting Summary

Nature Portfolio wishes to improve the reproducibility of the work that we publish. This form provides structure for consistency and transparency in reporting. For further information on Nature Portfolio policies, see our Editorial Policies and the Editorial Policy Checklist.

Statistics

For all statistical analyses, confirm that the following items are present in the figure legend, table legend, main text, or Methods section.

n/a	Confirmed	
☐	☒	The exact sample size (*n*) for each experimental group/condition, given as a discrete number and unit of measurement
☐	☒	A statement on whether measurements were taken from distinct samples or whether the same sample was measured repeatedly
☐	☒	The statistical test(s) used AND whether they are one- or two-sided *Only common tests should be described solely by name; describe more complex techniques in the Methods section.*
☒	☐	A description of all covariates tested
☐	☒	A description of any assumptions or corrections, such as tests of normality and adjustment for multiple comparisons
☐	☒	A full description of the statistical parameters including central tendency (e.g. means) or other basic estimates (e.g. regression coefficient) AND variation (e.g. standard deviation) or associated estimates of uncertainty (e.g. confidence intervals)
☐	☒	For null hypothesis testing, the test statistic (e.g. *F*, *t*, *r*) with confidence intervals, effect sizes, degrees of freedom and *P* value noted *Give P values as exact values whenever suitable.*
☒	☐	For Bayesian analysis, information on the choice of priors and Markov chain Monte Carlo settings
☒	☐	For hierarchical and complex designs, identification of the appropriate level for tests and full reporting of outcomes
☐	☒	Estimates of effect sizes (e.g. Cohen's *d*, Pearson's *r*), indicating how they were calculated

Our web collection on statistics for biologists contains articles on many of the points above.

Software and code

Policy information about availability of computer code

Data collection	All software used for data collection and analysis are described in detail in the Methods section, and a Jupyter notebook which takes readers step-by-step through the process is available at https://github.com/felixjwong/senolyticsai. Briefly, Chemprop (https://github.com/chemprop/chemprop, commit 9c8ff4074bd89b93f43a21adc49b458b0cab9e7f) and RDKit (version 2021.09.01) were used to build the graph neural networks as described in the Methods section. scikit-learn (https://scikit-learn.org/stable/, version 1.0) was used to build the random forest classifier models and for t-SNE visualization. AutoDock Vina 1.2.0, AutoDockTools 1.5.7, and PyMOL 2.5.2 were used to perform molecular docking and docking-related analyses. Manufacturer software from Molecular Devices (SoftMax Pro 6) for the SpectraMax M3 and SpectraMax M5 was used for plate reader measurements. ImageJ ver. 2.0.0-rc-69/1.52p was used for image analyses.
Data analysis	RDKit (https://www.rdkit.org/, version 2021.09.01) was used for cheminformatics. MATLAB (R2019b, Mathworks) was used for data processing.

For manuscripts utilizing custom algorithms or software that are central to the research but not yet described in published literature, software must be made available to editors and reviewers. We strongly encourage code deposition in a community repository (e.g. GitHub). See the Nature Portfolio guidelines for submitting code & software for further information.

Data

Policy information about availability of data

All manuscripts must include a data availability statement. This statement should provide the following information, where applicable:
- Accession codes, unique identifiers, or web links for publicly available datasets
- A description of any restrictions on data availability
- For clinical datasets or third party data, please ensure that the statement adheres to our policy

> Data generated from chemical screens, machine learning models, and computational analyses are available as Supplementary Data 1 to 4. For molecular docking studies, protein structures from accession codes 6qgh (Bcl-2), 3wiz (Bcl-XL), 1osf (Hsp90), 4hg7 (MDM2), and 4f1s (PI3K) were obtained from the Protein Data Bank at https://www.rcsb.org/. All other data are available from the corresponding author upon request.

Field-specific reporting

Please select the one below that is the best fit for your research. If you are not sure, read the appropriate sections before making your selection.

☒ Life sciences ☐ Behavioural & social sciences ☐ Ecological, evolutionary & environmental sciences

For a reference copy of the document with all sections, see nature.com/documents/nr-reporting-summary-flat.pdf

Life sciences study design

All studies must disclose on these points even when the disclosure is negative.

Sample size	No sample size calculation was performed, and sample sizes were typically determined based on the availability of experimental data. All data from all experiments were considered.
Data exclusions	No data were excluded for all experiments, with the exception of data from one mouse in each arm in the senescence-associated beta-galatosidase staining experiment shown in Fig. 6e. There, as discussed in the Methods section, one kidney sample from each of the vehicle- and BRD-K56819078-treated aged mice groups failed to stain for SA-β-gal, which may arise if the sections did not contain any kidney cortical region (ref. 86); data from these samples were discarded and not shown in Fig. 6e.
Replication	All data were representative of at least two biological replicates performed on at least one occasion, and the numbers of replications of each experiment are indicated as relevant. All attempts at replication were successful.
Randomization	There were no preallocation considerations. For mouse experiments, no significant bias was observed across initial groups.
Blinding	As we were not aware of any potential sources of bias in our experiments, we were not blinded to allocation when performing experiments or performing measurements.

Reporting for specific materials, systems and methods

We require information from authors about some types of materials, experimental systems and methods used in many studies. Here, indicate whether each material, system or method listed is relevant to your study. If you are not sure if a list item applies to your research, read the appropriate section before selecting a response.

Materials & experimental systems

n/a	Involved in the study
☒	☐ Antibodies
☐	☒ Eukaryotic cell lines
☒	☐ Palaeontology and archaeology
☐	☒ Animals and other organisms
☒	☐ Human research participants
☒	☐ Clinical data
☒	☐ Dual use research of concern

Methods

n/a	Involved in the study
☒	☐ ChIP-seq
☒	☐ Flow cytometry
☒	☐ MRI-based neuroimaging

Eukaryotic cell lines

Policy information about cell lines

Cell line source(s)	As described in the Methods section, human lung fibroblast (IMR-90) cells were obtained from ATCC (CCL-186). Human embryonic kidney (HEK293) and liver carcinoma (HepG2) cells were obtained from ATCC (ATCC CRL-1573 and HB-8065).

Authentication	All cells were authenticated using STR profiling by the supplier, ATCC.
Mycoplasma contamination	All cells were assayed for mycoplasma contamination by the supplier, ATCC. Mycoplasma contamination was not detected.
Commonly misidentified lines (See ICLAC register)	No commonly misidentified cell lines were used in this study.

Animals and other organisms

Policy information about studies involving animals; ARRIVE guidelines recommended for reporting animal research

Laboratory animals	For the baseline experiment shown in Fig. 6a-c, young (6- to 8-week-old) and aged (90-week-old) female C57BL/6J mice were procured from The Jackson Laboratory and quarantined at least 2 days prior to use. For the experiment shown in Fig. 6d-f, aged (80-week-old) female C57BL/6J mice were procured from The Jackson Laboratory and quarantined at least 2 days prior to use. Animals were housed in a facility maintained at 20-26ºC ambient temperature, 40-65% relative humidity, and a 12:12 light-dark cycle. Enrichment devices were included in the animal environments as required and changed bi-weekly. All mice in this study were treated in accordance with protocol IS00000852-6, approved by Harvard Medical School Institutional Animal Care and Use Committee and the Committee on Microbiological Safety.
Wild animals	No wild animals were used in this study.
Field-collected samples	No field-collected samples were used in this study.
Ethics oversight	Studies were performed at the Wyss Institute at Harvard and approved by the Harvard Medical School IACUC.

Note that full information on the approval of the study protocol must also be provided in the manuscript.